

Structure and Variability of the Martian Ion Composition Boundary Layer

J. S. Halekas¹, J. P. McFadden², D. A. Brain³, J. G. Luhmann², G.A. DiBraccio⁴, J.E.P. Connerney⁴, D. L. Mitchell², B.M. Jakosky³

¹Department of Physics and Astronomy, University of Iowa, Iowa City, Iowa, USA.

²Space Sciences Laboratory, University of California, Berkeley, California, USA.

³Laboratory for Atmospheric and Space Physics, University of Colorado, Colorado, USA.

⁴NASA Goddard Space Flight Center, Greenbelt, Maryland, USA.

Corresponding author: Jasper Halekas (jasper-halekas@uiowa.edu)

Key Points:

- The ion composition boundary (ICB) where the majority species changes from protons to heavy ions has asymmetries in location and structure
- The ICB altitude varies with solar wind ram pressure but not other drivers, while the plasma properties at the ICB vary with season
- The ICB lies at or below the altitude where the normal magnetic pressure balances the solar wind ram pressure, regardless of conditions

This article has been accepted for publication and undergone full peer review but has not been through the copyediting, typesetting, pagination and proofreading process which may lead to differences between this version and the Version of Record. Please cite this article as doi: 10.1029/2018JA025866

Abstract

A complex boundary layer with a variety of charged particle and electromagnetic field signatures, including a transition between plasma predominantly of solar wind origin and plasma of planetary origin, lies between the Martian bow shock and the ionosphere. In this paper, we develop and utilize algorithms to autonomously identify and characterize this ion composition boundary (ICB), using data from the Mars Atmosphere and Volatile Evolution (MAVEN) mission. We find an asymmetric ICB with a larger average thickness, lower altitude, and lower velocity shear in the hemisphere where the solar wind motional electric field points outward, as a result of the asymmetry of the mass loading process. The ICB thickness scales with the magnetosheath proton gyroradius at the top of the boundary layer, but does not clearly vary with external drivers. The ICB location varies with solar wind ram pressure and crustal magnetic field strength, but does not clearly respond to solar wind Mach number or extreme ultraviolet irradiance. The ICB represents a distinct boundary for ion density and flow speed, but the magnetic field strength and direction typically do not vary significantly across the ICB. The plasma density and flow speed at the ICB vary seasonally, likely in response to variations in the neutral exosphere and/or atmosphere. However, the ICB on average remains at or below the altitude where pressure balance is achieved between the piled up magnetic field and the solar wind ram pressure, regardless of season or crustal magnetic field strength.

Plain Language Summary

Planets without global intrinsic magnetic fields like that of the Earth interact in a distinctly different manner with the solar wind, a hot ionized gas (known as a “plasma”) that flows out through our solar system from the Sun. The interaction region includes a complex boundary layer where plasma dominated by the light ions of the solar wind transitions to plasma mainly composed of heavy ions derived from the planetary atmosphere. This boundary layer forms an interface between solar and planetary matter, and processes that occur in this unique region can transfer energy from the fast solar wind particles to the initially slower atmospheric particles, leading to the escape of atmospheric species. We investigate this compositional transition at Mars, utilizing data from the Mars Atmosphere and Volatile Evolution (MAVEN) mission, to determine its location, structure, and response to external and internal influences.

1 Introduction

The earliest systematic explorations of the Mars-solar wind interaction by the Mars spacecraft [Bogdanov and Vaisberg, 1975; Vaisberg et al., 1992] revealed the existence of a boundary layer between the bow shock and the ionosphere across which the composition of the plasma changes from predominantly light solar wind ions to predominantly heavy planetary ions. This boundary layer, also encountered by Phobos-2, Mars Global Surveyor (MGS), Mars Express (MEX), and most recently the Mars Atmosphere and Volatile Evolution (MAVEN) mission [Jakosky et al., 2015], has a number of observable signatures in addition to the compositional transition [Rosenbauer et al., 1989; Riedler et al., 1989; Lundin et al., 1989]. These include a decrease in low frequency magnetic field fluctuations, an increase in magnetic field strength, a transition to a more “draped” magnetic field configuration, and a decrease in suprathermal electron flux [Acuña et al., 1998; Vignes et al., 2000; Bertucci et al., 2004, 2005a,b; Nagy et al., 2004]. The various observational signatures of the boundary layer have nearly the same average location [Vignes et al., 2000; Trotignon et al., 2006; Dubinin et al., 2008b; Xu et al., 2016; Matsunaga et al., 2017], though they do not necessarily coincide on each individual orbit [Matsunaga et al., 2017]. On the other hand,

the compositional boundary does not have the same location as either the photoelectron boundary (PEB) [Mitchell et al., 2001] or the ionopause [Duru et al., 2009; Vogt et al., 2015], which typically occur at lower altitudes when present.

The Martian boundary layer has some counterparts, as boundary layers with many similarities occur at other objects without a strong global magnetic field, including Venus and Titan [Vaisberg and Zelenyi, 1984; Nagy et al., 1990; Sauer et al., 1995; Szego et al., 1991, 1995; Szego, 2001; Bertucci et al., 2005a, 2011], as well as comets [Neubauer, 1987; Mazelle et al., 1989]. However, the unique Martian crustal magnetic fields [Acuña et al., 1999] influence the boundary, increasing its altitude over strongly magnetic regions [Brain et al., 2005; Edberg et al., 2008; Fang et al., 2017]. The crustal fields also globally influence magnetic field topology and draping in the Martian magnetosphere [Brain et al., 2007; Luhmann et al., 2015a, 2015b; DiBraccio et al., 2018] and might therefore also affect the physics and structure of the boundary layer, as they unquestionably do for the PEB [Xu et al., 2017; Garnier et al., 2017]. Therefore, the crustal fields make the Martian case different from any known analogue

In part due to the multitude of observational signatures, and in part due to differences in observational capabilities, the Martian boundary layer and/or its elements have gone by many names, including the “magnetopause” [Lundin et al., 1990], the “protonopause” [Sauer et al., 1995], the “ion composition boundary” (ICB) [Breus et al., 1991; Sauer et al., 1994, 1995], the “magnetosphere boundary” (MB) or “induced magnetosphere boundary” (IMB) [Dubinin et al., 2006a; Lundin et al., 2004], the “plasma mantle” [Szego, 2001; Dubinin et al., 2006a], the “magnetic pileup boundary” (MPB) [Acuña et al., 1998; Crider et al., 2002; Bertucci et al., 2004, 2005a, 2005b], the “pressure balance boundary” [Xu et al., 2016], and simply “the boundary” [Dubinin et al., 1996; Sauer and Dubinin, 2000]. In this manuscript, we wish to focus on the location and structure of the compositional transition, so we will utilize the term ion composition boundary (ICB) or simply boundary layer in the succeeding pages. We base this choice purely on clarity and convenience, without judgment for the relative merits of the various boundary names.

The formation of the ICB is intimately related to mass loading [Szego et al., 2000], a process integral to the Mars-solar wind interaction. The addition of mass and momentum to the plasma through ionization of planetary neutral particles, together with the effects of crustal magnetic fields and induced currents in the ionosphere, results in the deceleration of the plasma and the commensurate pile up and draping of the solar wind magnetic field around the ionospheric source. The magnetic pressure associated with the compressed field (as well as crustal fields) balances the thermal pressure in the magnetosheath, which in turn balances the upstream solar wind ram pressure [Crider et al., 2003; Ma et al., 2004; Boesswetter et al., 2004; Dubinin et al., 2008a,b; Brain et al., 2010; Najib et al., 2011]. The piled up field therefore constitutes a magnetic barrier that forms the primary obstacle to the incident solar wind, ultimately determining the size and shape of the bow shock and of the magnetosheath through which the shocked solar wind flows around the magnetosphere.

It is not obvious that a continuous process such as mass loading should lead to well-defined boundaries. However, simulations and theoretical analyses suggest that mass loading cannot continuously proceed past a threshold mixing ratio, typically where the densities of solar wind and planetary ions become comparable, resulting in the formation of critical points in the flow [Sauer et al., 1992, 1994, 1995; Sauer and Dubinin, 2005; Dubinin et al., 2006c]. Therefore, boundary layers should naturally form around ionization sources such as the Martian ionosphere.

For a localized and non-uniform source such as the Martian ionosphere, the solar wind and newly born planetary ions initially have a relative velocity. Mass loading therefore results in plasma instabilities driven by the relative streaming of the different plasma populations, which can generate high-frequency waves in the boundary layer region [Grard et al., 1989; Trotignon et al., 1996] that can transfer energy from the solar wind to the planetary plasma.

In the presence of a magnetic field, the relative streaming of the ion populations also leads to the development of an asymmetric interaction, thanks to the directionality of the Lorentz force. Since solar wind and planetary ions initially have a relative velocity with respect to each other, they also stream with respect to the electrons, which flow at the speed needed to neutralize the total ion charge (the average ion flow speed). Therefore, both solar wind and planetary ions feel an electric field force due to their motion with respect to the magnetic field carried with the electrons. Initially, planetary ions flow slower than the electrons and solar wind ions, and therefore they experience an electric field that accelerates them and deflects them in the direction of the solar wind motional electric field E_m . In order to conserve momentum, the faster solar wind ions must then experience a counteracting electric field in their reference frame that decelerates them and deflects them in the direction opposite to E_m . Over longer time periods, the resulting momentum exchange will lead to a rotation of the two ion fluids around each other in velocity space; however, at Mars a full rotation may not occur until far downstream from the planet. These processes, which multi-fluid magnetohydrodynamics (MHD), hybrid, or fully kinetic equations can all at least in part describe, have been discussed by, among others, Sauer et al. [1994], Chapman and Dunlop [1986], Szego et al. [2000], Dubinin et al. [2011], and more recently by Halekas et al. [2017b].

As shown in Fig. 1, the asymmetric Lorentz force should lead to predictable asymmetries in both the location and structure of the ICB in Mars-Solar-Electric (MSE) coordinates (defined by the solar wind velocity v_{sw} , the perpendicular component of the solar wind magnetic field B_{sw} , and the solar wind motional electric field $E_m = -v_{sw} \times B_{sw}$, and calculated as in Halekas et al. [2017a]). The acceleration of planetary heavy ions in the $+E_m$ direction, which forms the observed ion “plume” [Dubinin et al., 2006d; Dong et al., 2014; Dong et al., 2015], leads to a corresponding deflection of the solar wind in the $-E_m$ direction (also seen at comets [Nilsson et al., 2015; Behar et al., 2016]) and therefore should cause a deflection of the ICB toward the $-E_m$ direction in the flanks of the magnetosphere. In addition, we expect asymmetries in the thickness of the ICB. As shown in Fig. 1, the pressure gradient forces on solar wind ions point inward in both hemispheres, while the pressure gradient forces on heavy ions point outward in both hemispheres. On the other hand, the motional electric field force on the solar wind ions points inward in the $+E_m$ hemisphere and outward in the $-E_m$ hemisphere, while for heavy ions it points outward in the $+E_m$ hemisphere, and inward in the $-E_m$ hemisphere. As a result, we expect a thicker ICB in the $+E_m$ hemisphere where all forces act to accelerate the two ion populations across the boundary and to mix them, and a thinner ICB in the $-E_m$ hemisphere where the electric field forces act to prevent the two populations from crossing the boundary and to keep them separated. Observations from MAVEN appear to support this expectation [Vaisberg et al., 2018]. Magnetic pressure and tension ($J \times B$) forces, as well as electric field forces due to electron pressure gradients, both of which act more symmetrically on the two ion populations, will also play a role in the overall interaction.

Boesswetter et al. [2004] and Simon et al. [2007] made similar arguments regarding the asymmetry of the ICB, and showed hybrid simulation results consistent with these expectations. Other Mars plasma simulations with appropriate physics included (for instance,

hybrid and multi-fluid MHD models) typically display similar features [Brecht and Ledvina, 2007; Najib et al., 2011; Dong et al., 2014; Modolo et al., 2006, 2016], albeit with differences in the details, as expected given the differences in implementation of the various models [Brain et al., 2010; Egan et al., 2018]. One of our primary purposes in this study is to determine whether MAVEN observations can confirm or disprove these expected asymmetries. In addition, we wish to understand the structure of the ICB and how it varies with external drivers and seasons.

2 Boundary Layer Observations and Location

Thanks to its comprehensive suite of plasma instrumentation, MAVEN provides the most complete set of measurements of the ICB since the Phobos-2 mission, and its elliptical orbit and high time resolution (in particular, significantly higher cadence than previous ion measurements) provide frequent and precise measurements of the boundary location and structure. Several authors [Matsunaga et al., 2017; Fang et al., 2017; Gruesbeck et al., 2018] have already used the combined set of MAVEN measurements to locate and characterize boundaries, utilizing multiple datasets and a mix of automated and manual procedures to identify each individual boundary crossing. In this work, we develop algorithms to autonomously identify and characterize the structure of the ICB using a robust subset of the available measurements, enabling rapid automated analysis of a large number of observations, as also performed for a previous analysis of the bow shock [Halekas et al., 2017a].

We identify and characterize the ICB by utilizing the ion composition ratio $n_p/(n_p + n_{O_2})$, calculated from partial ion densities measured by STATIC [McFadden et al., 2015] for protons and atomic and molecular oxygen ions (the three most abundant ion species at the altitudes of interest). This definition represents a choice based on physical considerations and computational convenience, which could result in biasing the boundary inward in the downstream flanks as compared to other possible definitions [Xu et al., 2016]. We utilize the STATIC 'c6' product (energy-mass histograms, with no angular resolution, but the highest possible time resolution) to compute all quantities. We do not include ions with mass per charge of two due to the overlap between solar wind He^{++} and planetary H_2^+ , and we do not attempt to separate minor ion species such as C^+ or CO_2^+ , which require fitting to separate from the main ion peaks [Inui et al., 2018]. The density ratio as we have defined it still contains ambiguity as to the origin of the ions, since H^+ ions (protons) have both solar wind and planetary sources. However, our testing indicates that this ratio works adequately to determine the location where the ion composition transitions from primarily solar wind origin to primarily planetary origin, since planetary H^+ typically comprises only a small percentage of the ion density inside the ICB.

Fig. 2 shows MAVEN data returned by the STATIC [McFadden et al., 2015] and MAG [Connerney et al., 2015a,b] instruments on four successive orbits. During this time period, MAVEN's orbit was oriented such that it crossed the inbound ICB above the dayside surface, at solar zenith angles (SZA) of 30-50° and altitudes of several hundred km, and the outbound ICB deep in the flanks, at SZA of 130-150° and altitudes of thousands of km. MAVEN briefly entered the solar wind in the upstream segment of several of the orbits, and passed through the dayside ionosphere and the downstream magnetotail on each orbit. The relatively low magnetic field values ($< \sim 30$ nT) observed during each periapsis indicate the absence of significant crustal magnetic fields at the periapsis locations.

In the upstream solar wind, we note the presence of background from contamination of heavy ion channels by internal scattering of solar wind protons, visible as narrow bands at

the solar wind energy in the heavy ion spectra. This background does not affect the subsequent analyses, since the ICB fits described below do not incorporate data from the solar wind, so we make no effort to remove it. The ion energy spectra in Fig. 2 do not incorporate corrections for spacecraft charging. However, the calculations of partial ion densities, as well as flow speeds (not shown in Fig. 2), do incorporate corrections for the effects of spacecraft charging.

We select the time intervals around ICB crossings, by identifying time periods when the density ratio goes from below 0.1 to above 0.9 (arbitrarily chosen thresholds), or vice versa. In order to avoid spurious identifications of boundaries associated with brief excursions in the density ratio (e.g. the plasmashet crossing at ~11:30 in Fig. 2), we impose a persistence requirement, analyzing only prospective ICB crossings where the density ratio remains above or below the threshold values for at least 50 samples (corresponding to 200 s at nominal sampling rates) before and after the crossing. After this initial identification stage, we further reject all but the outermost of any multiple ICB crossings in any given one-hour interval (for MAVEN's ~4.5 hour orbit, ICB crossings should not occur more frequently than this threshold), and all ICB crossings for which the measured density ratio does not increase with altitude. This comes at the cost of removing the cases with the largest fluctuations in boundary position and the most extreme cases of boundary layer instabilities, but this selection step proved necessary in order to avoid spurious identifications. For the time interval shown in Fig. 2, these procedures successfully identify all the intervals with ICB crossings, while selecting no spurious crossings.

Once we identify the intervals surrounding ICB crossings, we fit the measured density ratio for a time period with twice the duration of the crossing interval (the time range with the density ratio between 0.1 and 0.9, with the additional time around the crossing interval added to help constrain the fit at the endpoints) to a hyperbolic tangent function of the form $f(t) = A_0 + A_1 \tanh\left(\frac{t-A_2}{A_3}\right)$, using a gradient-expansion algorithm [Marquardt, 1963]. Fig. 2 shows the resulting fits along with the measured density ratio. We identify A_2 as the time at which the spacecraft crosses the ICB, and $2A_3$ as the temporal width of the ICB (the "crossing time" shown in Fig. 2). This width corresponds to the time span during which the density ratio varies over ~76% of the full range from minimum to maximum. We reject all fits with the dimensionless fit parameters A_0 or $|A_1|$ (the center value and height of the function) less than 0.33 or greater than 0.66 as unphysical. We evaluate the fit quality using the standard error (shown in Fig. 2), which for the un-weighted fit that we employ equals the square root of the chi-squared value. For the great majority of ICB crossings, the standard error does not exceed 0.2, indicating relatively good fits regardless of the crossing location.

By employing these algorithms for the entire time period 27 Nov 2014 to 27 Jan 2018, we identify and fit the density ratio for 9613 ICB crossings, an average of 8.3 per day. Given that MAVEN orbits Mars ~5.3 times per day, our algorithms successfully identify and fit 78% of ICB crossings, sufficient for accurate statistical characterization of the ICB location and properties.

In Fig. 2, we note a clear trend towards shorter crossing times for the dayside (inbound) ICB crossings and longer crossing times for the flank (outbound) ICB crossings, which also holds for the entire data set. To better quantify this trend and rule out geometric effects related to the spacecraft orbit rather than geophysical causes, we must determine the spatial thickness of the ICB. We could calculate a first order estimate by simply multiplying the temporal width $2A_3$ by the spacecraft velocity; however, this would not account for the angle of incidence with respect to the boundary surface. With a single point measurement, we cannot determine the boundary surface normal a priori for each crossing. However, we can

define a nominal boundary surface and use the angle of incidence with respect to that nominal surface to estimate an approximate spatial thickness for each ICB crossing.

To accomplish this, we consider the distribution of ICB crossings, as shown in Fig. 3. Rather than defining an asymmetric surface to represent the ICB (as done for the bow shock by Gruesbeck et al. [2018]), we utilize a symmetric surface for computational simplicity and convenience. The exact functional form of this surface has no particular physical significance, and we use it only to determine the relative location of the ICB and to estimate its thickness. Using the MPB fit of Trotignon et al. [2006] as a starting point, we define a nominal ICB surface using two conic sections. For $x > 0$, we use a very similar conic section with the same focus ($0.64 R_M$), a slightly larger eccentricity (0.8 rather than 0.77), and a slightly smaller semi-latus rectum (1.0 rather than 1.08). For $x < 0$, we utilize a conic section with the same focus ($1.64 R_M$) but a significantly lower eccentricity (0.93 rather than 1.01, close to the eccentricity value of 0.9 from Vignes et al. [2000]) and higher semi-latus rectum (0.62 rather than 0.53). This conic section better represents the ICB, at least as observed during the MAVEN mission.

The ICB determined by our analysis does not flare outward in the downstream flanks of the magnetosphere, but appears to continue straight or even curve inward downstream from the planet, particularly in the +z MSE hemisphere. Note that this difference in shape and the slightly lower altitude on the dayside as compared to the Trotignon et al. [2006] fits does not necessarily imply a difference in the ICB and MPB locations, since it could at least in part represent a temporal difference in the boundary location, given the different time periods studied. However, Matsunaga et al. [2017] found the ICB below the IMB/MPB on the night side using MAVEN observations, and Xu et al. [2016] found that in multi-fluid MHD simulations the ICB as we have defined it lies below boundaries defined by other methods, supporting a real difference.

Though we utilize a symmetric conic section for calculations, we do observe a clear systematic asymmetry in the location of the ICB, with the boundary shifted towards the -z MSE hemisphere, similar to the asymmetry found for the MPB by Edberg et al. [2009], and consistent with the predictions from momentum conservation considerations associated with mass loading discussed above in Section 1. We clearly see this asymmetry both in the average measured ion density ratio and in the spatial distribution of ICB crossings identified by our algorithms.

The ICB also deviates from this nominal surface in regions of strong crustal magnetism, as shown in Fig. 4. As demonstrated in previous studies [Crider et al., 2002; Brain et al., 2005; Edberg et al., 2008; Dubinin et al., 2008b; Matsunaga et al., 2017; Fang et al., 2017] and also found for the lower PEB [Garnier et al., 2017], the presence of the strong crustal magnetic fields in the southern far side of Mars clearly increases the altitude of the boundary when they lie on the dayside. However, we find that the strength of the total (draped + crustal) magnetic field at the center of the ICB remains roughly constant as a function of spacecraft location, suggesting that the dayside ICB remains closely tied to the altitude of pressure balance [Xu et al., 2016] regardless of the presence or absence of crustal fields.

3 Boundary Layer Structure

An advantage of our autonomous method for ICB identification lies in its ability to provide an objective estimate not only of the boundary location but also its thickness. As mentioned above, we initially perform our fitting using time as the independent variable, so we must convert the crossing time to a spatial thickness by utilizing the spacecraft velocity

component normal to the boundary. We estimate this normal velocity by assuming that the instantaneous ICB surface normal lies close to the normal at the closest point on the nominal boundary surface of Fig. 3. While this may not hold exactly true on every single crossing, it should prove reasonably accurate for most cases, allowing the investigation of statistical trends.

We find that the ICB thicknesses so derived range from tens to hundreds of km ($0.003\text{-}0.06 R_M$) on the dayside, but can reach values of up to a few thousand km ($0.6 R_M$) in the downstream flanks. While the simulation results of Xu et al. [2016] suggest boundary layer thicknesses roughly two times larger, this discrepancy likely results largely from a different definition of the thickness.

In order to characterize the thickness of the ICB in terms of the local plasma quantities, we compute the proton and heavy ion gyroradii at the inner and outer edges of the ICB from the local magnetic field strength measured by MAG and the average scalar ion speed $|v|$ for each species measured by STATIC (the gyroradius we use thus contains both thermal and bulk ion velocity components). We utilize an average heavy ion gyroradius computed from the average speed for O^+ and O_2^+ ions and an average mass of 24. The ICB thickness correlates closely with both the proton and heavy ion gyroradii, particularly those at the outer edge of the ICB, as shown in Fig. 5. We find linear correlation coefficients of 0.3-0.5 and rank correlations of 0.4-0.5 between the ICB thickness and both the heavy ion and proton gyroradii at the outer edge of the ICB. One might guess that these correlations could arise fortuitously because both ICB thickness and ion gyroradius increase with SZA (the latter because the magnetic field strength at the boundary decreases with SZA). However, if we take subsets of data from smaller SZA ranges, we actually find much higher correlation coefficients for dayside crossings, with linear correlation coefficients of ~ 0.7 for crossings at SZA of $0\text{-}60^\circ$ (or subsets thereof). On the other hand, downstream crossings have much lower linear correlation coefficients of only 0.15-0.2.

While the ICB thickness correlates well with both proton and heavy ion gyroradii, we find typical values considerably smaller than the heavy ion gyroradius scale, but close to the proton gyroradius scale. The ICB properties therefore appear consistent with a scenario wherein the local magnetosheath proton gyroradius at the outer edge of the ICB primarily determines its thickness on the dayside, while the downstream ICB forms an expansion fan with a thickness that does not depend strongly on the local ion gyroradius.

As discussed above in Section 1 and shown in Fig. 1, considerations of the electric field and pressure gradient forces lead to the prediction that the ICB should have a larger thickness in the hemisphere where the solar wind motional electric field E_m points upward, and a narrower thickness in the opposite hemisphere. To search for such an asymmetry, we plot the thickness of the ICB as a function of the location of the crossing with respect to the $+E_m$ direction, as shown in Fig. 6. We do indeed find larger ICB thicknesses (by a factor of ~ 2) in the $+E_m$ hemisphere at all SZA, confirming expectations from basic principles and simulations [Boesswetter et al., 2004; Simon et al., 2007]. This asymmetry becomes even more pronounced when normalizing the thickness by the proton gyroradius, as a result of the stronger magnetic field pileup observed in the $+E_m$ hemisphere of Mars [Vennerstrom et al., 2003; Dubinin et al., 2006a; Harada et al., 2015; Halekas et al., 2017b]. On the other hand, as shown in Fig. 6, there is no clear organization of the thickness of the ICB by MSO coordinates, indicating that the strong crustal magnetic fields in the southern hemisphere do not have a clear effect on the structure of the boundary. Furthermore, we find no clear asymmetry in the X-Y MSO plane (given the nominal Parker spiral IMF geometry, $+Y$ or MSO clock angle of 0 corresponds to the quasi-perpendicular flank, and $-Y$ or MSO clock

angle of 180 to the quasi-parallel flank of the magnetosphere). Even when considering only specific individual IMF sectors (not shown), we still do not find a clear ICB asymmetry in the plane of the IMF.

We next consider the structure of the boundary layer in terms of basic plasma quantities. Given previous studies indicating that the ICB location lies close to if not exactly contiguous to the MPB [Matsunaga et al., 2017], one might expect to observe an increase in magnetic field magnitude across the ICB. However, as shown in Fig. 7, the magnetic field at the inner edge of the ICB barely exceeds that at the outer edge, with an average magnetic field magnitude ratio equal to unity except for the crossings with the weakest fields (primarily located on the downstream flanks). This suggests that either the ICB lies below the MPB on average, and/or that the ion composition transition has a considerably smaller average thickness than the magnetic field magnitude transition. The latter appears unlikely, since Bertucci et al. [2005a] estimated MPB thicknesses on the order of ~ 80 km at 60° SZA, comparable to the ICB thicknesses we derive in the same region. Therefore, the compositional transition may in fact lie at or below the location of maximum magnetic field pileup. This appears consistent with the simulation results of Boeswetter et al. [2004], which found the ICB coincident with a plateau in the magnetic field strength rather than an altitude range with strong gradients in field magnitude.

We also find that the magnetic field does not typically rotate significantly across the ICB, and that it does not typically have a large component normal to the nominal ICB surface, as shown in Fig. 7. This suggests that the field on average has a nominal draped geometry [Cridler et al., 2004] at both the inner and outer edge of the boundary, again consistent with a location below the MPB, where observations have indicated more draped field geometry [Bertucci et al., 2003]. The degree of magnetic field rotation across the boundary and the deviation of the field from perfect draping do not appear related to the ratio between the field magnitude at the inner and outer edges of the boundary, nor do they show any clear trend with SZA.

As expected, the densities of both protons and heavy ions change dramatically across the ICB, as shown in Fig. 8. Given our definition of the boundary, the heavy ion density should increase inward except in very unusual circumstances, and our results confirm this expectation. The proton density need not decrease inward across the ICB, given that the total ion density increases dramatically; however, we find that it does so in the majority of cases, suggesting that the ICB typically stops much or all of the solar wind flow. Those cases where the proton density does not decrease inward very likely result from the addition of planetary hydrogen ions.

The ICB also represents a flow boundary, as shown in Fig. 8. Both proton and heavy ion speeds decrease inward across the ICB in the vast majority of boundary crossings, regardless of SZA. The former result stands in contrast to the results of Boeswetter et al. [2004], which predicted an increase in proton velocity just below the ICB; however, that simulation did not include planetary hydrogen ions, which may in part account for the discrepancy. While it is not obvious that both protons and heavy ions should slow across the boundary, this behavior appears consistent with previous observations and the hypothesis that the boundary forms by processes related to mass loading.

The ion flow speeds at the ICB also display asymmetries in MSE coordinates, with larger differences in the average ion flow speed between the inner and outer edge of the ICB in the $-z$ MSE hemisphere, as shown in Fig. 8. This asymmetry likely results from the same considerations discussed in Section 1, which lead to a narrower and sharper boundary with less mixing of populations across it, favorable for the development of flow shears. We note

that larger flow shear could lead a higher incidence of boundary instabilities such as “plasma clouds” [Halekas et al., 2016] and Kelvin-Helmholtz [Penz et al., 2004; Ruhunusiri et al., 2016] in the -z MSE hemisphere, with implications for boundary layer structure and bulk escape processes.

4 Boundary Layer Pressure Balance

We now consider the pressure balance at the ICB, by comparing the normal component of the solar wind ram pressure to the normal magnetic pressure associated with the total (draped + crustal) magnetic field in the barrier. Similar to Crider et al. [2003], we assume Newtonian pressure balance. In a gas-dynamic approximation, the ram pressure transmitted through the sheath and exerted on the boundary $p_{normal} = 0.88\rho_{sw}v_{sw}^2\cos^2\theta$, with θ the angle between the solar wind flow and the local boundary normal, and the normalization constant 0.88 corresponding to the pressure at the stagnation point. However, this formula neglects the thermal and magnetic pressure carried in the solar wind, and therefore gives unphysical results in the flanks, as θ tends to zero. To correct for this, we utilize the prescription of Sotirelis [1996] to add a term ensuring that the normal pressure at the boundary asymptotes to the non-ram portion of the solar wind pressure at the flanks. We utilize the expression $p_{normal} = 0.88\rho_{sw}v_{sw}^2\cos^2\theta + p_{sw}\sin^2\theta$ to estimate the normal pressure at the ICB, computing θ from the nominal ICB surface of Fig. 3, utilizing the total mass density (protons + alpha particles) of the solar wind to compute the ram pressure, and summing the solar wind thermal pressure and magnetic pressure to compute the upstream pressure p_{sw} . We compute the total normal magnetic pressure at the barrier $p_{B,normal} = B_{tangential}^2/(2\mu_0)$, again using the nominal ICB surface to determine the tangential field component. Neglecting gradients other pressure terms such as thermal plasma pressure at the ICB, these two pressures should balance, assuming the Newtonian approximation holds (note that significant pressure anisotropy and/or non-zero off-diagonal terms in the pressure tensor could invalidate this assumption).

We find that the normal component of the magnetic pressure on average (albeit with significant variability about the average) balances the normal component of the solar wind pressure at the ICB over the entire dayside for a wide range of conditions, as shown in Fig. 9. This suggests that the ICB on average lies at the altitude where pressure balance is first achieved, or somewhere below this altitude (since the magnetic pressure presumably does not increase beyond that needed to achieve pressure balance at lower altitudes, except in regions with strong crustal fields). This appears consistent with the results of Boeswetter et al. [2004], who predicted that the maximum pileup of the magnetic field occurs at the location of the ICB.

On the other hand, even with the inclusion of the non-ram components of the solar wind pressure, the normal pressure does not on average balance at the ICB in the downstream flanks, with the magnetic pressure typically larger than the solar wind pressure. This suggests that other terms may play a greater role in the force balance across the ICB in the flanks, and/or that the pressure balance surface lies at a higher altitude than the ICB in the downstream region, as predicted by Xu et al. [2016].

5 Boundary Layer Dependence on External Drivers

Previous work has indicated that the MPB does not respond to external drivers in the same way as the bow shock. The bow shock moves inward during times with high solar wind ram pressure or magnetosonic Mach number, and outward during times with high EUV [Edberg et al., 2009, 2010; Halekas et al 2017a]. Similarly, the MPB/MB moves inward

during times with high solar wind ram pressure [Crider et al., 2003; Brain et al., 2005; Dubinin et al., 2006a; Edberg et al., 2009]. Surprisingly, since higher EUV irradiance increases the altitude of the ionosphere and should thus lead to an increase in the altitude of the boundary layer, Edberg et al. [2009] instead found that the MPB moves inward during times with high EUV. We investigate the ICB location as a function of these same three drivers, all of which MAVEN measures, in Fig. 10. For ram pressure and magnetosonic Mach number, we utilize the methodology of Halekas et al. [2017a] to extract upstream parameters from SWIA [Halekas et al., 2015] and MAG [Connerney et al., 2015a, 2015b] measurements (only for orbits that crossed the ICB and also entered the upstream solar wind), while for EUV we utilize Lyman alpha irradiance measurements from the EUVM instrument (available for nearly all orbits) [Eparvier et al., 2015].

In agreement with previous work, we find that the ICB position depends strongly on solar wind ram pressure, moving inward during periods of higher ram pressure at all SZA. This trend flattens out at lower ram pressure, suggesting an effective maximum size for the magnetosphere, at least during the MAVEN mission. On the other hand, the boundary location continues to move inward up to the highest ram pressure values observed, suggesting that at least during the MAVEN mission we have not reached a minimum magnetospheric size threshold. We find no clear dependence of the ICB location on the upstream magnetosonic Mach number at any SZA, in contrast to the behavior of the bow shock [Edberg et al., 2010; Halekas et al., 2017a]. We also find no clear trend of ICB position with EUV irradiance, also in contrast to the bow shock, and in contrast to previous results [Edberg et al., 2009]. We find this lack of a trend surprising, given the importance of mass loading in the formation of the ICB. However, the correlation between EUV irradiance and solar wind ram pressure due to the $1/r^2$ effect of heliocentric distance might mask a positive correlation with EUV.

We also find no strong trends in ICB thickness as a function of any of the three external drivers considered. A very weak apparent anti-correlation of thickness with solar wind ram pressure probably appears because of the correlation between solar wind ram pressure and magnetic field strength, which influences the ion gyroradius.

6 Boundary Layer Seasonal Variability

Lastly, we consider the seasonal variation of the ICB's location and properties. The Mars-solar wind interaction has known seasonal variations, in large part due to the seasonal variability in the exosphere. Recent observations have shown that the high altitude neutral hydrogen exosphere of Mars increases in column density by approximately an order of magnitude during southern summer (which occurs shortly after Mars' perihelion, at solar longitude $L_S \sim 270$) [Chaffin et al., 2014; Bhattacharyya et al., 2015; Yamauchi et al., 2015; Halekas, 2017]. This increase in neutral density results in a commensurate increase in the production of H^+ ions [Rahmati et al., 2018], primarily by charge exchange [Kallio et al., 1997]. While charge exchange with neutral hydrogen does not increase the average mass of the flowing ions, it decreases their average flow speed, and therefore still constitutes a mass loading (or more correctly momentum loading) process. The replacement of fast solar wind ions by cold hydrogen ions slows and deflects the solar wind flow even upstream of the bow shock [Halekas et al., 2017a], and affects the foreshock, bow shock, and magnetosheath [Dubinin et al., 2006b, 2018]. Given the higher exospheric neutral densities at lower altitudes, this loading of the flow could significantly affect the interaction in the vicinity of the ICB.

Heavy neutral species, on the other hand, exhibit somewhat different seasonal variations. The column density of the high-altitude neutral oxygen exosphere, and thus the

flux of O^+ pickup ions from photoionization and charge exchange, do not appear to increase significantly near perihelion [Rahmati et al., 2018]. However, both the density and flux of low energy O^+ ions at lower altitudes of ~200-600 km increase by as much as an order of magnitude during high EUV conditions such as those encountered near perihelion [Dubinin et al., 2017]. This significant increase in heavy ion density at lower altitudes could also affect the interaction in the vicinity of the ICB.

Indeed, our observations indicate dramatic differences in the ion properties at the ICB during the time period around perihelion and southern summer, as shown in Fig. 11. The average proton and heavy ion density at the ICB increase by a factor of four to eight for all SZA, with the peak densities occurring at $L_S \sim 270-300$ near southern summer (slightly after perihelion, which takes place at $L_S \sim 251$), with a time profile quite similar to that observed for exospheric hydrogen column density [Halekas, 2017]. Meanwhile, the average proton flow speed at the ICB decreases by a similar factor during the same time period. The heavy ion flow speed, on the other hand, shows only a slight decrease. At the same time, the average altitude of the ICB shows no clear changes other than those associated with the variable coverage of the downstream flanks afforded by the MAVEN orbit. Furthermore, the average ratio between the normal component of the magnetic pressure and the normal component of the solar wind pressure at the ICB, calculated as described above in Section 4, shows no clear variability with season, consistent with an approximately constant ICB altitude.

The observations in Fig. 11 indicate that the location of the ICB remains relatively constant with season, occurring at or below the altitude where the total (draped + crustal) magnetic field on the dayside achieves pressure balance with the solar wind ram pressure, regardless of the ion density. However, the incident proton density at this location increases significantly, while the incident flow speed decreases significantly. The heavy ion density increases commensurately with the incident proton density, while the flow speed decreases only slightly, which in combination results in the large increase in cold heavy ion escape flux described by Dubinin et al. [2017].

One can imagine several different scenarios that could lead to the seasonal variability seen in Fig. 11. First, lower altitude influences could drive the variability in the interaction, with higher heavy ion densities at low altitudes leading to a change in the boundary layer. In this case one might expect the ICB to move upward in order to maintain the same density at the boundary, rather than taking place at a higher density level. Alternatively, higher altitude influences could drive the variability in the interaction, with the increase in mass loading due to the higher exospheric hydrogen density leading to a more dense and slower incident proton flow. In this case one might expect the ICB to move lower in altitude, where the heavy ion density would balance the higher proton density.

Given that we observe no clear seasonal changes in the altitude of the ICB, we cannot differentiate between the two scenarios outlined above, though the observed time profile may slightly favor the scenario where influences from above related to the hydrogen exosphere drive the observed variability. On the other hand, both effects may play a role, and they may to some degree counteract each other in their influence on the boundary altitude.

Furthermore, the altitude of pressure balance is intimately related the altitude of the compositional transition, and so the physics of the interaction may ensure that the compositional transition on average occurs at or below the altitude at which pressure balance is achieved, regardless of the value of the plasma density. This scenario seems plausible, given the consistency in the pressures observed at the ICB. It may seem unclear why the compositional transition should occur at an altitude related to the pressure balance altitude.

However, the pile up of the magnetic field and the compositional change occur in part due to the same processes. The magnetic field and the solar wind protons initially flow together, along with the solar wind electrons. As mass loading occurs, the magnetic field carried by the electrons initially lags behind the protons, and the flow slows, leading to an increase in density and magnetic field strength, and a decrease in flow speed. In addition, the electron fluid changes from purely solar wind electrons to an admixture of solar wind electrons and cold electrons created by photoionization and electron impact ionization. As the incident protons slow and ultimately deflect and/or reflect in the magnetic barrier, the magnetic field strength should reach its maximum, in a self-consistent manner. The presence of crustal magnetic fields may of course perturb this interaction; however, the results of Fig. 2 suggest that they simply shift the boundary layer to a higher altitude.

7 Conclusions

The excellent coverage of the Mars-solar wind interaction provided by the MAVEN mission and the high time resolution of the STATIC instrument allow us to precisely determine the location, characteristics, and variability of the ion composition boundary. Although the ICB is only one aspect of a complex boundary layer with a number of observable signatures, we have focused in this work on the compositional transition and the altitude where the pressure associated with the piled up magnetic field balances the solar wind ram pressure.

We find that the compositional transition on average lies at or below the altitude where this pressure balance is accomplished, regardless of solar zenith angle, crustal magnetic field strength, solar wind conditions, or season. This holds true despite significant asymmetries in the interaction, variations of the ICB location in response to both external drivers and crustal magnetic fields, and seasonal variability of the plasma characteristics at the boundary. This suggests that the compositional transition and the magnetic field pileup occur self consistently as part of the mass loading process, as expected from basic physical considerations. The unique Martian crustal magnetic fields significantly perturb the location of the compositional boundary, but do not obviously change its characteristics. The plasma at the boundary changes dramatically with season, likely in response to changes in the neutral exosphere and/or atmosphere, but this surprisingly does not appear to affect the altitude of the boundary or the pressure balance at that location. This supports a scenario where the pressure balance provides the defining characteristic of the boundary, with the location of the compositional transition closely tied to the altitude where pressure balance is accomplished.

The asymmetry of the ICB reflects the asymmetry of the mass loading process, and in turn suggests that asymmetries must also exist in the instabilities that occur at the boundary, in the processes that transfer energy between the solar wind and the planetary plasma, and ultimately in the escape of particles from the system. The most obvious manifestation of these asymmetries is the now well-known plume of ions escaping along the solar wind motional electric field direction. However, the higher velocity shear we find at the boundary in the opposite hemisphere may also have important implications for the development of instabilities and the bulk escape of plasma.

The basic characteristics of the ICB described in this manuscript largely agree with the results from hybrid and multi-fluid simulations, suggesting that these simulations can successfully capture the physics of the interaction. However, our observations provide a number of new observational constraints that can now be used to further validate the simulations. The computational capability now exists to run simulations for a variety of external conditions, allowing us to investigate the response of the system to changing solar

wind and seasonal conditions. While our observations will provide constraints for these simulations, the models can provide unmatched coverage of the interaction for each set of conditions, allowing us to go from the local measurements provided by spacecraft to a global perspective of the system.

Acknowledgments, Samples, and Data

We acknowledge the MAVEN contract for support. All MAVEN data are available on the Planetary Data System (<https://pds.nasa.gov>).

References

- Acuña, M. H., et al. (1998), Magnetic field and plasma observations at Mars: Initial results of the Mars Global Surveyor Mission, *Science*, 279, 1676–1680.
- Acuña, M.H., J.E.P. Connerney, N.F. Ness, et al. (1999), Global distribution of crustal magnetization found by the Mars Global Surveyor MAG/ER experiment, *Science*, 284, 790.
- Behar, E., H. Nilsson, G. Stenberg Wieser, Z. Nemeth, T. W. Broiles, I. Richter (2016), Mass loading at 67P/Churyumov-Gerasimenko: A case study, *Geophys. Res. Lett.*, 43, 1411–1418, doi:10.1002/2015GL067436.
- Bertucci, C. et al. (2004), MGS MAG/ER observations at the magnetic pileup boundary of Mars: draping enhancement and low frequency waves. *Adv. Space Res.*, 33, 1938–1944.
- Bertucci, C., C. Mazelle, M. H. Acuña, C. T. Russell, J. A. Slavin (2005a), Structure of the magnetic pileup boundary at Mars and Venus, *J. Geophys. Res.*, 110, A01209, doi:10.1029/2004JA010592.
- Bertucci, C., C. Mazelle, and M. Acuña (2005b), Structure and variability of the Martian magnetic pileup boundary and bow shock from MGS MAG/ER observations, *Adv. Space. Res.*, 36(11), 2066–2076, doi:10.1016/j.asr.2005.05.096.
- Bertucci, C., F. Duru, N. Edberg, M. Fraenz, C. Martinecz, K. Szego, O. Vaisberg (2011), The induced magnetospheres of Mars, Venus, and Titan, *Space Sci. Rev.*, 162, 113–171.
- Bhattacharyya, D., J. T. Clarke, J.-L. Bertaux, J.-Y. Chaufray, and M. Mayyasi (2015), A strong seasonal dependence in the Martian hydrogen exosphere, *Geophys. Res. Lett.*, 42, 8678–8685, doi:10.1002/2015GL065804.
- Boesswetter, A., T. Bagdonat, U. Motschmann, K. Sauer (2004), Plasma boundaries at Mars: A 3-D simulation study, *Ann. Geophys.*, 22, 4363-4379.
- Bogdanov, A. V., and O. L. Vaisberg (1975), Structure and variations of solar wind-Mars interaction region, *J. Geophys. Res.*, 80, 487–494, doi: 10.1029/JA080i004p00487.

- Brain, D. A., J. S. Halekas, R. J. Lillis, D. L. Mitchell, R. P. Lin, D. H. Crider (2005), Variability of the altitude of the Martian sheath, *Geophys. Res. Lett.*, *32*, L18203, doi:10.1029/2005GL023126.
- Brain, D., R. Lillis, D. Mitchell, J. Halekas, R. Lin (2007), Electron pitch angle distributions as indicators of magnetic field topology near Mars, *J. Geophys. Res.*, *112*, A09201, doi:10.1029/2007JA012435.
- Brain, D., et al. (2010), A comparison of global models for the solar wind interaction with Mars, *Icarus*, *206*, 149–151, doi:10.1016/j.icarus.2009.06.030.
- Brecht, S. H., and S. A. Ledvina (2007), The solar wind interaction with the Martian ionosphere/atmosphere, *Space Sci. Rev.*, *126*, 15–38.
- Breus, T. K., A. M. Krymskii, R. Lundin, E. M. Dubinin, J. G. Luhmann, Y. G. Yeroshenko, S. V. Barabash, V. Y. Mitnitskii, N. F. Pissarenko, V. A. Styashkin (1991), The solar wind interaction with Mars: Consideration of Phobos-2 mission observation of an ion composition boundary on the dayside, *J. Geophys. Res.*, *96*, 11165-11174.
- Chaffin, M. S., J.-Y. Chaufray, I. Stewart, F. Montmessin, N.M. Schneider, J.-L. Bertaux (2014), Unexpected variability of Martian hydrogen escape, *Geophys. Res. Lett.*, *41*, 314-320.
- Chapman, S. C., and M. W. Dunlop (1986), Ordering of momentum transfer along VvB in the AMPTE solar wind releases, *J. Geophys. Res.*, *91*, 8051-8055.
- Connerney, J., J. Espley, P. Lawton, S. Murphy, J. Odom, R. Oliverson, D. Sheppard (2015a), The MAVEN magnetic field investigation, *Space. Sci. Rev.*, *195*, doi:10.1007/s11214-015-0169-4.
- Connerney, J. E. P., J. R. Espley, G. A. DiBraccio, J. R. Gruesbeck, R. J. Oliverson, D. L. Mitchell, J. Halekas, C. Mazelle, D. Brain, B. M. Jakosky (2015b), First results of the MAVEN magnetic field investigation, *Geophys. Res. Lett.*, *42*, 88198827, doi:10.1002/2015GL065366.
- Crider, D.H., Acuña, M.H., Connerney, J.E.P., et al. (2002), Observations of the latitude dependence of the location of the Martian magnetic pileup boundary, *Geophys. Res. Lett.*, *29*, 11–1–11-4.
- Crider, D. H., D. Vignes, A. M. Krymskii, T. K. Breus, N. F. Ness, D. L. Mitchell, J. A. Slavin, M. Acuña (2003), A proxy for determining solar wind dynamic pressure at Mars using Mars Global Surveyor data, *J. Geophys. Res.*, *108*, 1461, doi:10.1029/2003JA009875.
- Crider, D., D.A. Brain, M. Acuña, D. Vignes, C. Mazelle, C. Bertucci (2004), Mars Global Surveyor observations of solar wind magnetic field draping around Mars, *Space Sci. Rev.* *111*, 203–221.

DiBraccio, G. A., Luhmann, J. G., Curry, S. M., Espley, J. R., Xu, S., Mitchell, D. L., et al. (2018). The twisted configuration of the Martian magnetotail: MAVEN observations. *Geophys. Res. Lett.*, *45*.

<https://doi.org/10.1029/2018GL077251>

Dong, C., S. W. Bougher, Y. Ma, G. Toth, A. F. Nagy, D. Najib (2014), Solar wind interaction with Mars upper atmosphere: Results from the one-way coupling between the multifluid MHD model and the MTGCM model, *Geophys. Res. Lett.*, *41*, 2708–2715, doi:10.1002/2014GL059515.

Dong, Y., X. Fang, D.A. Brain, J.P. McFadden, J.S. Halekas, J.E. Connerney, S. Curry, Y. Harada, J.G.

Luhmann, B.M. Jakosky (2015), Strong plume fluxes at Mars observed by MAVEN: An important planetary ion escape channel, *Geophys. Res. Lett.*, *42*, doi:10.1002/2015GL065346.

Dubinin, E., K. Sauer, R. Lundin, O. Norberg, J-G. Trotignon, K. Schwingenschuh, M. Delva, W. Riedler

(1996), Plasma characteristics of the boundary layer in the Martian magnetosphere, *J. Geophys. Res.*, *101*, 27061-27075.

Dubinin, E., M. Franz, J. Woch, E. Roussos, S. Barabash, R. Lundin, J.D. Winningham, R.A. Frahm, M. Acuna

(2006a), Plasma morphology at Mars: ASPERA-3 observations, *Space Sci. Rev.*, *126*, 209-238.

Dubinin, E., M. Fraenz, J. Woch, S. Barabash, R. Lundin, M. Yamauchi (2006b), Hydrogen exosphere at Mars:

Pickup protons and their acceleration at the bow shock, *Geophys. Res. Lett.*, *33*, L22103,

doi:10.1029/2006GL027799.

Dubinin, E. M., K. Sauer, J. F. McKenzie (2006c), Nonlinear 1-d stationary flows in multi-ion plasmas? sonic

and critical loci? Solitary and “oscillatory waves, *Annal. Geophys.*, *24*, 3041-3057.

Dubinin, E., et al. (2006d), Electric fields within the Martian magnetosphere and ion extraction: ASPERA-3

observations, *Icarus*, *182*, 337–342, doi:10.1016/j.icarus.2005.05.022.

Dubinin, E., R. Modolo, M. Fraenz, J. Woch, F. Duru, F. Akalin, D. Gurnett, R. Lundin, S. Barabash, J.J. Plaut,

G. Picardi (2008a), Structure and dynamics of the solar wind/ionosphere interface on Mars: MEX-

ASPERA-3 and MEX-MARSIS observations, *Geophys. Res. Lett.*, *35*, L11103,

doi:10.1029/2008GL033730.

Dubinin, E., et al. (2008b), Plasma environment of Mars as observed by simultaneous MEX-ASPERA-3 and

MEX-MARSIS observations, *J. Geophys. Res.*, *113*, A10217, doi:10.1029/2008JA013355.

Dubinin, E., M. Fraenz, A. Fedorov, R. Lundin, N. Edberg, F. Duru, O. Vaisberg (2011), Ion energization and

escape on Mars and Venus, *Space Sci. Rev.*, *162*, 173.

- Dubinin, E., M. Fraenz, M. Pätzold, J. McFadden, P. R. Mahaffy, F. Eparvier, J. S. Halekas, J. E. P. Connerney, D. Brain, B. M. Jakosky, O. Vaisberg, L. Zelenyi (2017), Effects of solar irradiance on the upper ionosphere and oxygen ion escape at Mars: MAVEN observations, *J. Geophys. Res.*, *122*, 7142-7152.
- Dubinin, E., Fraenz, M., Pätzold, M., Halekas, J. S., Mcfadden, J., Connerney, J. E. P., et al. (2018). Solar wind deflection by mass loading in the Martian magnetosheath based on MAVEN observations. *Geophys. Res. Lett.*, *45*, 2574–2579, doi:10.1002/2017GL076813.
- Duru, F., D. A. Gurnett, R. A. Frahm, J. D. Winningham, D. D. Morgan, G. G. Howes (2009), Steep, transient density gradients in the Martian ionosphere similar to the ionopause at Venus, *J. Geophys. Res.*, *114*, A12310, doi:10.1029/2009JA014711.
- Egan, H., Y. Ma, C. Dong, R. Modolo, R. Jarvinen, S. Bougher, et al. (2018), Comparison of global Martian plasma models in the context of MAVEN observations, *J. Geophys. Res.*, *123*, doi:10.1029/2017JA025068.
- Edberg, N. J. T., M. Lester, S. W. H. Cowley, A. I. Eriksson (2008), Statistical analysis of the location of the martian magnetic pileup boundary and bow shock and the influence of crustal magnetic fields, *J. Geophys. Res.*, *113*, A08206, doi:10.1029/2008JA013096.
- Edberg, N., D. A. Brain, M. Lester, S. W. H. Cowley, R. Modolo, M. Fraenz, S. Barabash (2009), Plasma boundary variability at Mars as observed by Mars Global Surveyor and Mars Express, *Ann. Geophys.*, *27*, 3537–3550.
- Edberg, N. J. T., M. Lester, S. W. H. Crowley, D. A. Brain, M. Franz, S. Barabash (2010), Magnetosonic Mach number effect of the position of the bow shock at Mars in comparison to Venus, *J. Geophys. Res.*, doi:10.1029/2009JA014998.
- Eparvier, F. G., P. C. Chamberlin, T. N. Woods, E. M. B. Thiemann (2015), The Solar Extreme Ultraviolet Monitor for MAVEN, *Space Sci. Rev.*, *195*, 293–301, doi:10.1007/s11214-015-0195-2.
- Fang, X., Y. Ma, K. Masunaga, Y. Dong, D. Brain, J. Halekas, R. Lillis, B. Jakosky, J. Connerney, J. Grebowsky, C. Dong (2017), The Mars crustal magnetic field control of plasma boundary locations and atmospheric loss: MHD prediction and comparison with MAVEN, *J. Geophys. Res.*, *122*, 4117–4137, doi:10.1002/2016JA023509.
- Garnier, P., Steckiewicz, M., Mazelle, C., Xu, S., Mitchell, D., Holmberg, M. K. G.,... Jakosky, B. M. (2017). The Martian photoelectron boundary as seen by MAVEN, *J. Geophys. Res.*, *122*, 10,472–10,485.
- Grad, R., Pedersen, A., Klimov, S., Savin, S., Skalsky, A., Trotignon, J. G., Kennel, C. (1989), First Measurements of plasma waves near Mars, *Nature*, *341*, 607.

- Gruesbeck, J. R., Espley, J. R., Connerney, J. E. P., DiBraccio, G. A., Soobiah Y. I., D. Brain, et al. (2018). The three-dimensional bow shock of Mars as observed by MAVEN. *J. Geophys. Res.*, *123*, <https://doi.org/10.1029/2018JA025366>.
- Halekas, J.S., E.R. Taylor, G. Dalton, G. Johnson, D.W. Curtis, J.P. McFadden, D.L. Mitchell, R.P. Lin, B.M. Jakosky (2015), The Solar Wind Ion Analyzer for MAVEN, *Space. Sci. Rev.*, *195*, 125-151, doi:10.1007/s11214-013-0029-z.
- Halekas, J. S., D. A. Brain, S. Ruhunusiri, J. P. McFadden, D. L. Mitchell, C. Mazelle, J. E. P. Connerney, Y. Harada, T. Hara, J. R. Espley, G.A. Dibraccio, B.M. Jakosky (2016), Plasma clouds and snowplows: Bulk plasma escape from Mars observed by MAVEN, *Geophys. Res. Lett.*, *43*, doi:10.1002/2016GL067752.
- Halekas, J. S. (2017), Seasonal variability of the hydrogen exosphere of Mars, *J. Geophys. Res.*, *122*, doi:10.1002/2017JE005306.
- Halekas, J. S., et al. (2017a), Structure, dynamics, and seasonal variability of the Mars-solar wind interaction: MAVEN Solar Wind Ion Analyzer in-flight performance and science results, *J. Geophys. Res.*, *122*, 547–578, doi:10.1002/2016JA023167.
- Halekas, J. S., Brain, D. A., Luhmann, J. G., DiBraccio, G. A., Ruhunusiri, S., Harada, Y., ... Jakosky, B. M. (2017b). Flows, fields, and forces in the Mars-solar wind interaction. *J. Geophys. Res.*, *122*, 11,320–11,341.
- Harada, Y., J.S. Halekas, J.P. McFadden, D.L. Mitchell, C. Mazelle, J.E.P. Connerney, J. Espley, D.E. Larson, D.A. Brain, G.A. DiBraccio, S.M. Curry, T. Hara, R. Livi, S. Ruhunusiri, B.M. Jakosky (2015), Marsward and tailward ions in the near-Mars magnetotail: MAVEN observations, *Geophys. Res. Lett.*, *42*, doi:10.1002/2015GL065005.
- Inui, S., K. Seki, T. Namekawa, S. Sakai, D. A. Brain, T. Hara, J. P. McFadden, J. S. Halekas, D. L. Mitchell, C. Mazelle, G. A. DiBraccio, B. M. Jakosky (2018), Cold dense ion outflow observed in the Martian induced magnetotail by MAVEN, *Geophys. Res. Lett.*, doi:10.1029/2018GL077584.
- Jakosky, B.M., R.P. Lin, J.M. Grebowsky, et al. (2015), The Mars Atmosphere and Volatile Evolution (MAVEN) mission, *Space Sci. Rev.*, *195*, doi:10.1007/s11214-015-0139-x.
- Kallio, E., J.G. Luhmann, S. Barabash (1997), Charge exchange near Mars: Solar wind absorption and energetic neutral atom production, *J. Geophys. Res.*, *102*, 22183-22197.
- Luhmann, J. G., Y. J. Ma, D. A. Brain, D. Ulusen, R. J. Lillis, J. S. Halekas, J. R. Espley (2015a), Solar wind interaction effects on the magnetic fields around Mars: Consequences for interplanetary and crustal field measurements, *Planet. Space Sci.*, *117*, 15–23.

- Luhmann, J. G., et al. (2015b), Implications of MAVEN Mars near-wake measurements and models, *Geophys. Res. Lett.*, *42*, 9087–9094, doi:10.1002/2015GL066122.
- Lundin, R., Zakharov, A., Pellinen, R., Borg, H., Hultqvist, B., Pissarenko, N., Dubinin, E. M., Barabash, S. V., Liede, I., Koskinen, H. (1989), First measurements of the ionospheric plasma escape from Mars, *Nature*, *341*, 6243, 609.
- Lundin, R., A. Zakharov, R. Pellinen, H. Borg, B. Hultqvist, N. Pissarenko, E. M. Dubinin, S. W. Barabash, I. Liede, H. Koskinen (1990), Plasma composition measurements of the Martian magnetosphere morphology, *Geophys. Res. Lett.*, *17*, 877–880.
- Lundin, R., S. Barabash, H. Andersson, M. Holmström, et al. (2004), Solar wind induced atmospheric erosion at Mars—First results from ASPERA-3 on Mars Express, *Science*, *305*, 1933-1936.
- Ma, Y., A. F. Nagy, I. V. Sokolov, K. C. Hansen (2004), Three-dimensional, multispecies, high spatial resolution MHD studies of the solar wind interaction with Mars, *J. Geophys. Res.*, *109*, A07211, doi:10.1029/2003JA010367.
- Marquardt, D.W. (1963), An algorithm for least-squares estimation of nonlinear parameters", *J. Soc. Ind. Appl. Math.*, *11*, 431-441.
- Matsunaga, K., K. Seki, D. A. Brain, T. Hara, K. Masunaga, J. P. Mcfadden, J. S. Halekas, D. L. Mitchell, C. Mazelle, J. R. Espley, J. Gruesbeck, B. M. Jakosky (2017), Statistical study of relations between the induced magnetosphere, ion composition, and pressure balance boundaries around Mars based on MAVEN observations, *J. Geophys. Res.*, *122*, 99723-9737.
- Mazelle, C., et al. (1989), Analysis of suprathermal electron properties at the magnetic pile-up boundary of comet P/Halley, *Geophys. Res. Lett.*, *16*, 1035 – 1038.
- McFadden, J., Kortmann, O., G. Dalton, G.J., R. Abiad, D. Curtis, R. Sterling, K. Hatch, P. Berg, C. Tiu, M. Marckwordt, R. Lin, B. Jakosky (2015), The MAVEN Suprathermal and thermal Ion Composition (STATIC) Instrument, *Space Sci. Rev.*, *195*, 199-256.
- Mitchell, D. L., et al. (2001), Probing Mars' crustal magnetic field and ionosphere with the MGS electron reflectometer, *J. Geophys. Res.*, *106*, 23,419–23,427.
- Modolo, R., G. Chanteur, E. Dubinin, A. P. Matthews (2006), Simulated solar wind plasma interaction with the Martian exosphere: Influence of the solar EUV flux on the bow shock and the magnetic pile-up boundary, *Ann. Geophys.*, *24*, 3403–3410.

- Modolo, R., et al. (2016), Mars-solar wind interaction: LatHyS, an improved parallel 3-D multispecies hybrid model, *J. Geophys. Res.*, *121*, 6378–6399, doi:10.1002/2015JA022324.
- Moses, S.L., F.V. Coroniti, F.L. Scarf (1988), Expectations for the microphysics of the Mars-solar wind interaction, *Geophys. Res. Lett.*, *15*, 429-432.
- Najib, D., A. F. Nagy, G. Tóth, Y. Ma (2011), Three-dimensional, multifluid, high spatial resolution MHD model studies of the solar wind interaction with Mars, *J. Geophys. Res.*, *116*, A05204, doi:10.1029/2010JA016272.
- Nagy, A. F., T. I. Gombosi, K. Szego, R. Z. Sagdeev, V. D. Shapiro, V. I. Shevchenko (1990), Venus mantle-Mars planetosphere - What are the similarities and differences?, *Geophys. Res. Lett.*, *17*, 865-868.
- Nagy, A.F., D. Winterhalter, K. Sauer, et al. (2004), The plasma environment of Mars, *Space Sci. Rev.*, *111*, 33.
- Neubauer, F. M. (1987), Giotto magnetic-field results on the boundaries of the pile-up region and the magnetic cavity, *Astron. Astrophys.*, *187*, 73–79.
- Nilsson, H., G. Stenberg-Wieser, E. Behar, et al. (2015), Evolution of the ion environment of comet 67P/Churyumov-Gerasimenko— Observations between 3.6 and 2.2 AU, *Astron. Astrophys.*, *538*, A20, doi:10.1051/0004-6361/201526142.
- Penz, T., et al. (2004), Ion loss on Mars caused by the Kelvin-Helmholtz instability, *Planet. Space Sci.*, *52*, 1157–1167.
- Rahmati, A., Larson, D. E., Cravens, T. E., Lillis, R. J., Halekas, J. S., McFadden, J. P., et al. (2018). Seasonal variability of neutral escape from Mars as derived from MAVEN pickup ion observations. *J. Geophys. Res.*, *123*, doi:10.1029/2018JE005560.
- Riedler, W., Mohlmann, D., Oraevsky, V. N., Schwingenschuh, K., Eroshenko, Ye., Rustenbach, J., Aydogar, Oe., Berghofer, G., Lichtenegger, H., Delva, M., Schelch, G., Pirsch, K., Fremuth, G., Steller, M., Arnold, H., Raditsch, T., Ayster, U., Fornacon, K.-H., Schenk, H. J., Michaelis, H., Motschmann, U., Roatsch, T., Sauer, K., Schroter, R., Kurths, J., Lenners, D., Linthe, J., Kobzev, V., Styashkin, V., Achache, J., Slavin, J., Luhmann, J. G., Russell, C. T.: 1989, Magnetic fields near Mars: First results, *Nature*, *341*, 604.
- Rosenbauer, H., N. Shutte, I. Apathy, A. Galeev, K. Gringauz, H. Gruenwaldt, P. Hemmerich, K. Jockers, P. Kiraly, G. Kotova, S. Livi, E. Marsh, A. Richter, W. Riedler, A. Remizov, R. Schwenn, K. Schwingenschuh, M. Steller, K. Szego, M. Verigin, M. Witte (1989), Ions of martian origin and plasma sheet in the martian magnetotail: Initial results of TAUS experiment, *Nature*, *341*, 612.

- Ruhunusiri, S., et al. (2016), MAVEN observations of partially developed Kelvin-Helmholtz vortices at Mars, *Geophys. Res. Lett.*, *43*, 4763–4773, doi:10.1002/2016GL068926.
- Sauer, K., T. Roatsch, K. Baumgärtel, J. F. McKenzie (1992), Critical density layer as obstacle at solar wind – exospheric ion interaction, *Geophys. Res. Lett.*, *19*, 645-648.
- Sauer, K., A. Bogdanov, K. Baumgärtel (1994), Evidence of an ion composition boundary (protonopause) in bi-ion fluid simulations of solar wind mass loading, *Geophys. Res. Lett.*, *21*, 153-158.
- Sauer, K., A. Bogdanov, K. Baumgärtel (1995), The protonopause – an ion composition boundary in the magnetosheath of comets, Venus and Mars, *Adv. Space Res.*, *16*, 2255-2258.
- Sauer, K., and E. Dubinin (2000), The nature of the Martian ‘obstacle boundary’, *Adv. Space Res.*, *26*, 1633-1637.
- Simon, S., A. Boesswetter, T. Bagdonat, U. Motschmann (2007), Physics of the ion composition boundary: A comparative 3-D hybrid simulation of Mars and Titan, *Ann. Geophys.*, *25*, 99-115.
- Sotirelis, T. (1996), The shape and field of the magnetopause as determined from pressure balance, *J. Geophys. Res.*, *101*, 15255-15264.
- Szego, K., V. S. Shapiro, V. I. Shevchenko, R. Z. Sagdeev, W. T. K. Kasprzak, A. F. Nagy (1991), Physical processes in the plasma mantle of Venus, *Geophys. Res. Lett.*, *18*, 2305-2308.
- Szegö, K., V.D. Shapiro, S.K. Ride, A.F. Nagy, V.I. Shevchenko (1995), The sheath/ionosphere boundary layer at Venus, *Adv. in Space Res.*, *16*, 71.
- Szego, K, K.-H. Glassmeier, R. Bingham, et al. (2000), Physics of mass loaded plasmas, *Space Sci. Rev.*, *94*, 429-671.
- Szego, K., Present understanding of the dayside mantle regions of Venus and Mars (2001), *Adv. Space Res.*, *28*, 841-850.
- Trotignon, J.-G., E. Dubinin, R. Grard, S. Barabash, R. Lundin (1996), Martian planetopause as seen by the plasma wave system onboard Phobos 2, *J. Geophys. Res.*, *101*, 24,965 – 24,977.
- Trotignon, J., C. Mazelle, C. Bertucci, M. Acuña (2006), Martian shock and magnetic pile-up boundary positions and shapes determined from the Phobos 2 and Mars Global Surveyor data sets, *Planet. Space Sci.*, *54*, 357-369, doi:10.1016/j.pss.2006.01.003.
- Vaisberg, O. L., and L. M. Zelenyi (1984), Formation of the plasma mantle in the Venusian magnetosphere, *Icarus*, *58*, 412-430.

Vaisberg, O. L (1992), The solar wind interaction with Mars: A review of results from previous Soviet missions to Mars, *Adv. Space Res.* *12*, 137–161.

Vaisberg, O. L., Ermakov, V. N., Shuvalov, S. D., Zelenyi, L. M., Halekas, J., DiBraccio, G. A., et al. (2018).

The structure of Martian magnetosphere at the dayside terminator region as observed on MAVEN spacecraft. *J. Geophys. Res.*, *123*, 2679–2695. <https://doi.org/10.1002/2018JA025202>

Vennerstrom, S., Olsen, N., Purucker, M., Acuna, M. H., and Cain, J. C. (2003), The magnetic field in the pile-up region at Mars, and its variation with the solar wind, *Geophys. Res. Lett.*, *30*, 1369– 1373.

Vignes, D., C. Mazelle, H. Reme, M. H. Acuna, J. E. P. Connerney, R. P. Lin, D. L. Mitchell, P. Cloutier, D. H.

Crider, N. F. Ness (2000), The solar wind interaction with Mars: Locations and shapes of the bow shock and the magnetic pile-up boundary from the observations of the MAG/ER experiment onboard Mars Global Surveyor, *Geophys. Res. Lett.*, *27*, 49 – 52.

Vogt, M. F., P. Withers, P. R. Mahaffy, M. Benna, M. K. Elrod, J. S. Halekas, J. E. P. Connerney, J. R. Espley,

D. L. Mitchell, C. Mazelle, B. M. Jakosky (2015), Ionopause-like density gradients in the Martian ionosphere: A first look with MAVEN, *Geophys. Res. Lett.*, *42*, 8885-8893.

Xu, S., M. W. Liemohn, C. Dong, D. L. Mitchell, S. W. Bougher, Y. Ma (2016), Pressure and ion composition boundaries at Mars, *J. Geophys. Res.*, *121*, 6417–6429, doi:10.1002/2016JA022644.

Xu, S., et al. (2017), Martian low-altitude magnetic topology deduced from MAVEN/SWEA observations, *J. Geophys. Res.*, *122*, 1831–1852, doi:10.1002/2016JA023467.

Yamauchi, M., T. Hara, R. Lundin, E. Dubinin, A. Fedorov, J.-A. Sauvaud, R. A. Frahm, R. Ramstad, Y.

Futaana, M. Holmstrom, S. Barabash (2015), Seasonal variation of Martian pick-up ions: Evidence of breathing exosphere, *Planet. Space Sci.*, doi:10.1016/j.pss.2015.09.013.

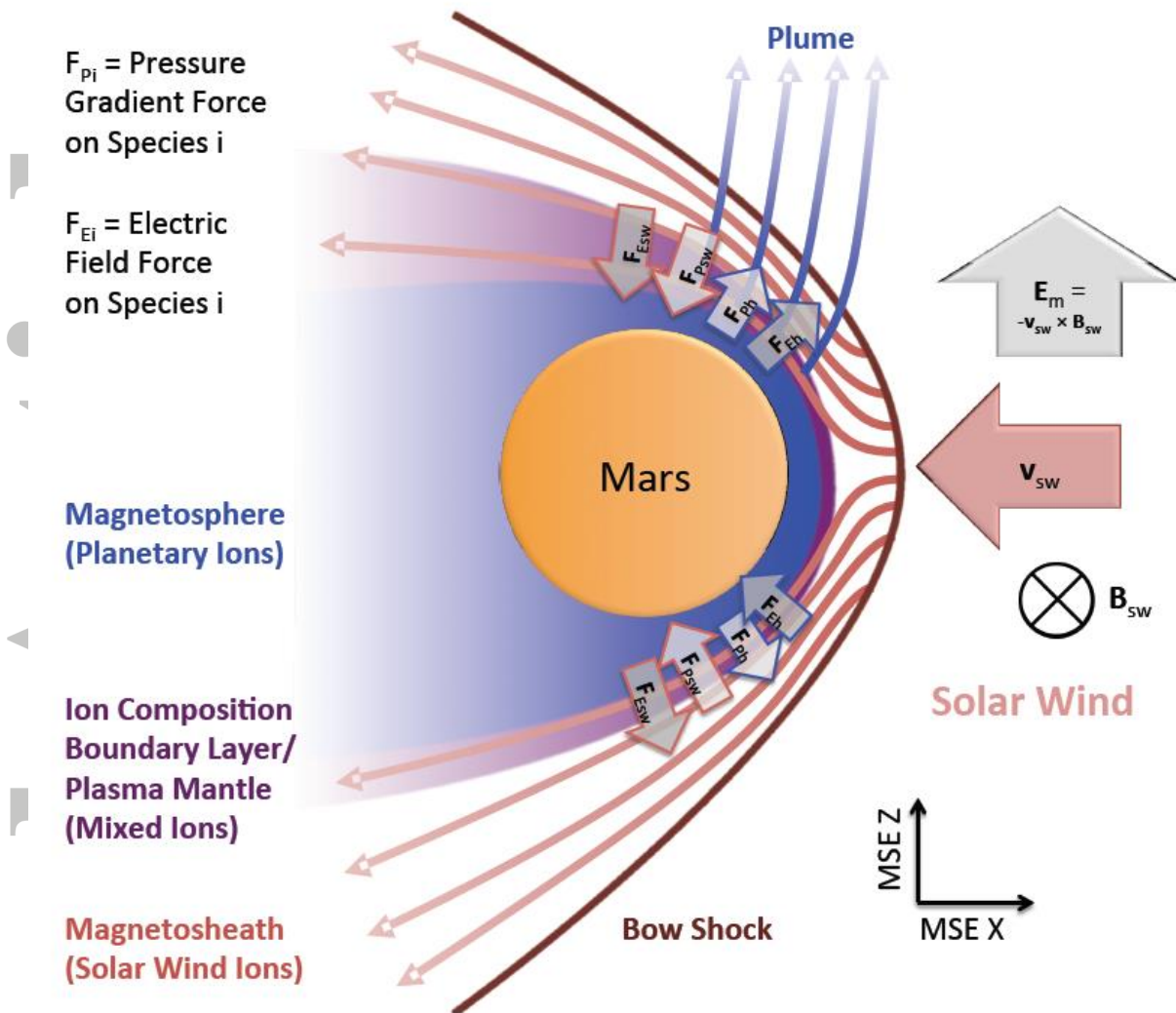


Figure 1: The Mars-solar wind interaction in MSE coordinates, with key regions, proton and heavy ion populations, and pressure gradient and electric field forces on these ion populations.

Accepted

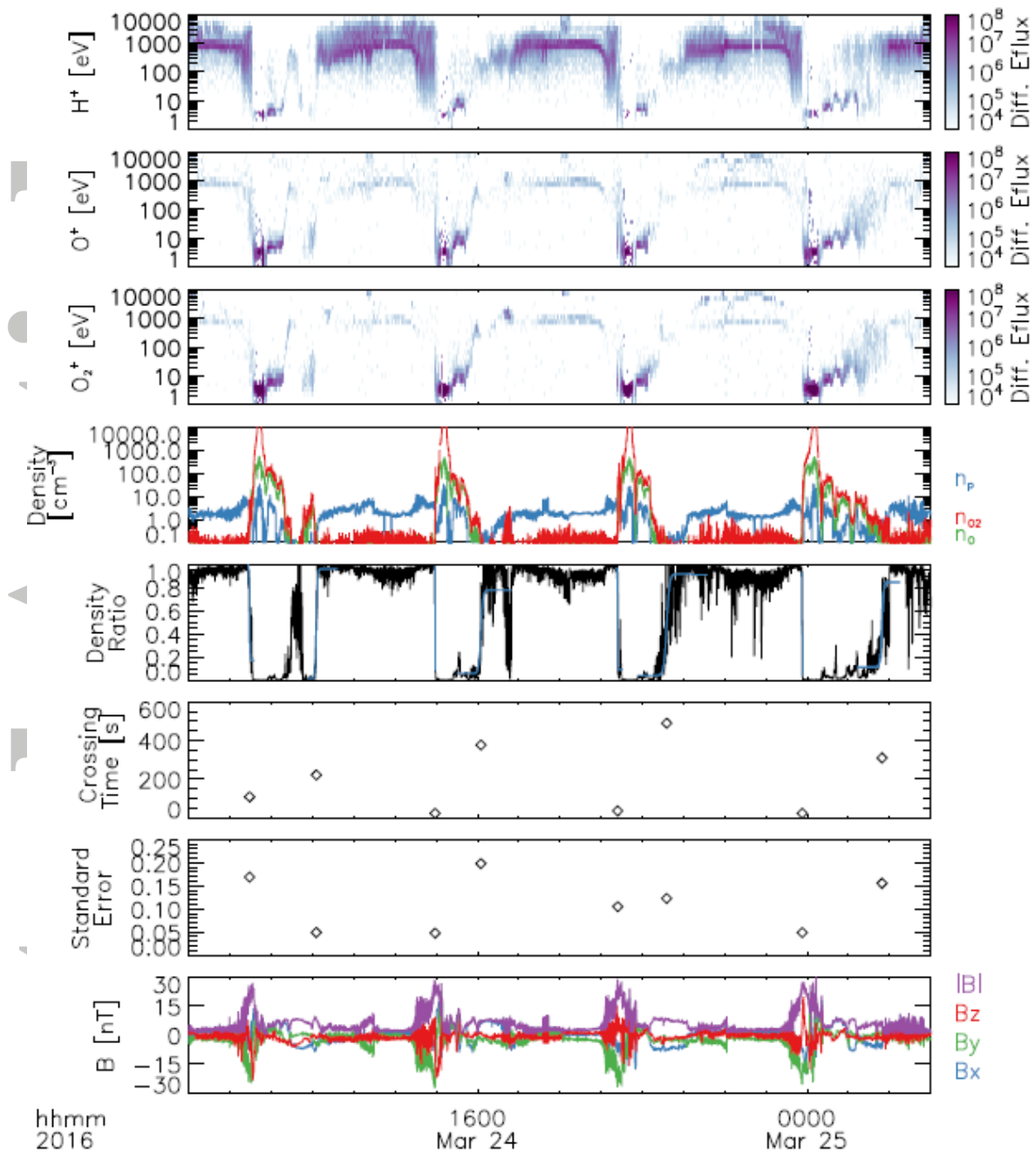


Figure 2: Hydrogen ion (proton), atomic oxygen ion, and molecular oxygen ion differential energy flux spectra in units of eV/[eV cm² s sr], corresponding ion densities (corrected for spacecraft potential), and the ion density ratio $n_p / (n_p + n_o + n_{O_2})$ measured by STATIC (black line), together with hyperbolic tangent function fits (blue lines), crossing times for each ICB computed from these fits, and the standard errors of the fits. For context, the bottom panel shows the vector magnetic field measured by MAG, in Mars-Solar-Orbital (MSO) coordinates.

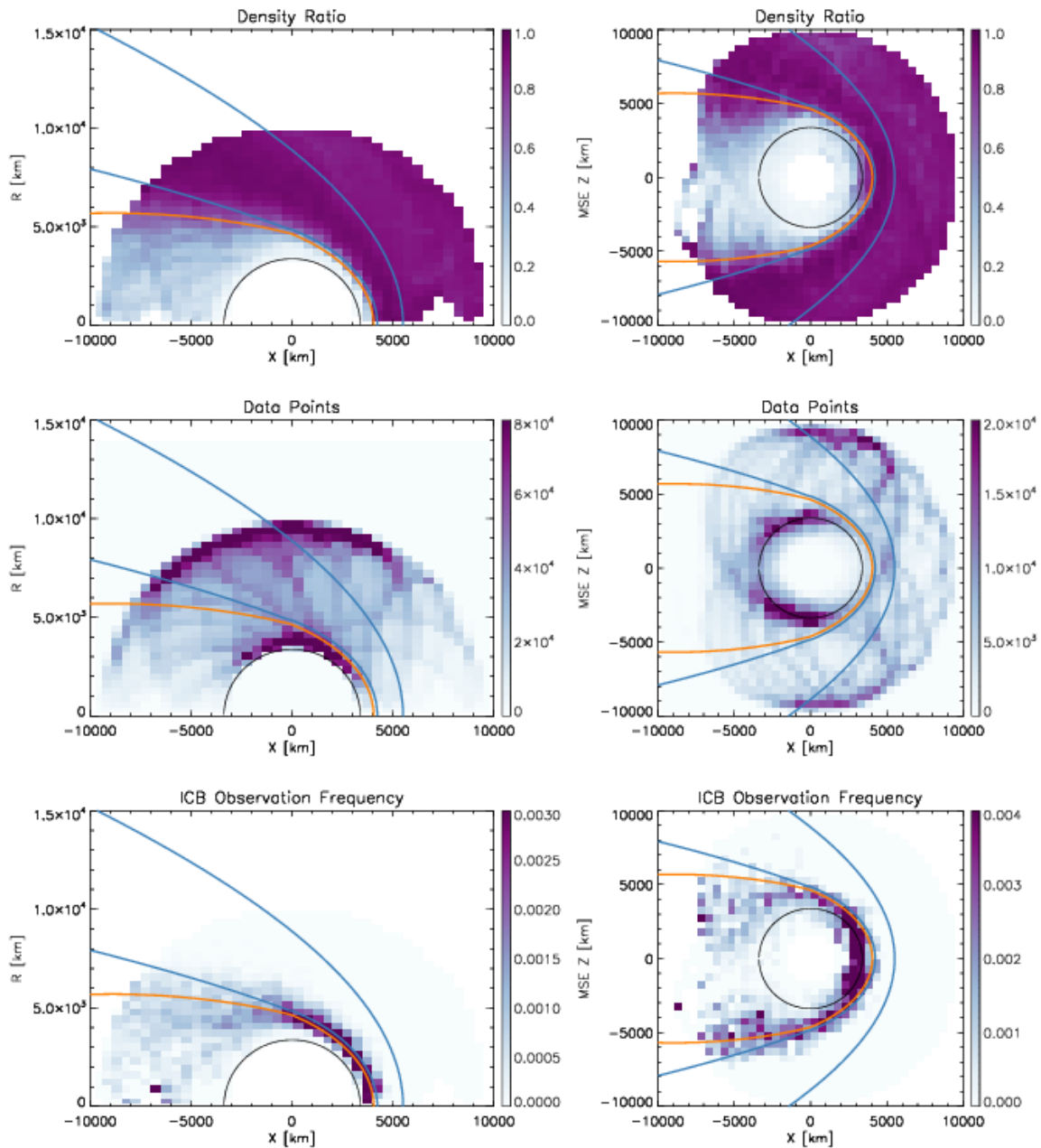


Figure 3: Average ion density ratio, STATIC data coverage, and ICB observation frequency (number of ICB crossings divided by number of data points), in cylindrical MSO coordinates (left column) and Cartesian MSE coordinates (right column, data from $|y| < 3000$ km projected to the x-z plane, only for orbits during which we also measure the upstream magnetic field). The blue curves show the nominal bow shock and MPB location from Trotignon et al. [2006]. The orange curves show the nominal ICB location used in this study.

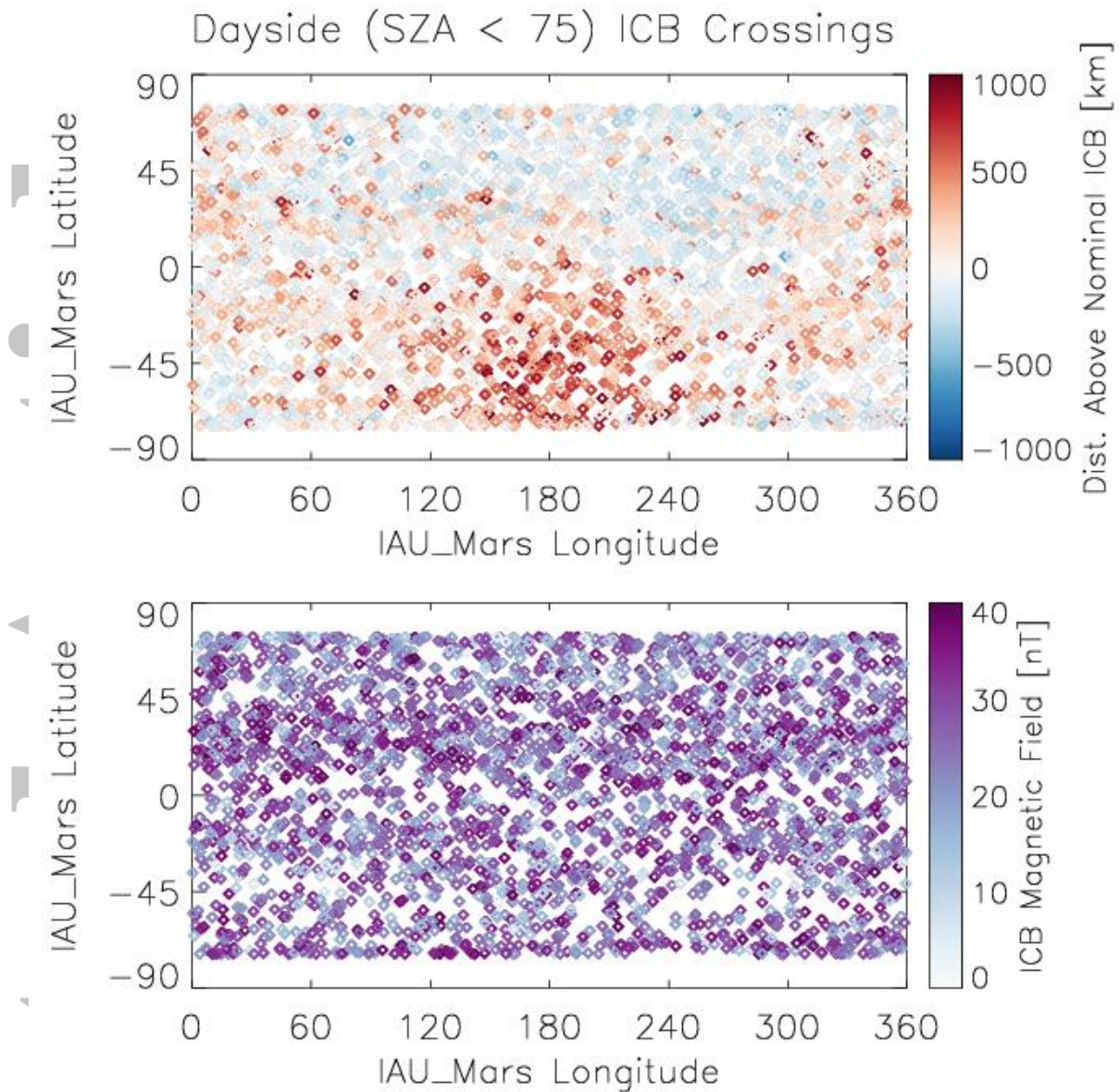


Figure 4: The distance of dayside ($SZA < 75^\circ$) ICB crossings above or below the nominal ICB surface of Fig. 3, and the total magnetic field strength at the center of the ICB, as a function of the Mars-fixed location directly below the spacecraft at the time of the ICB encounter.

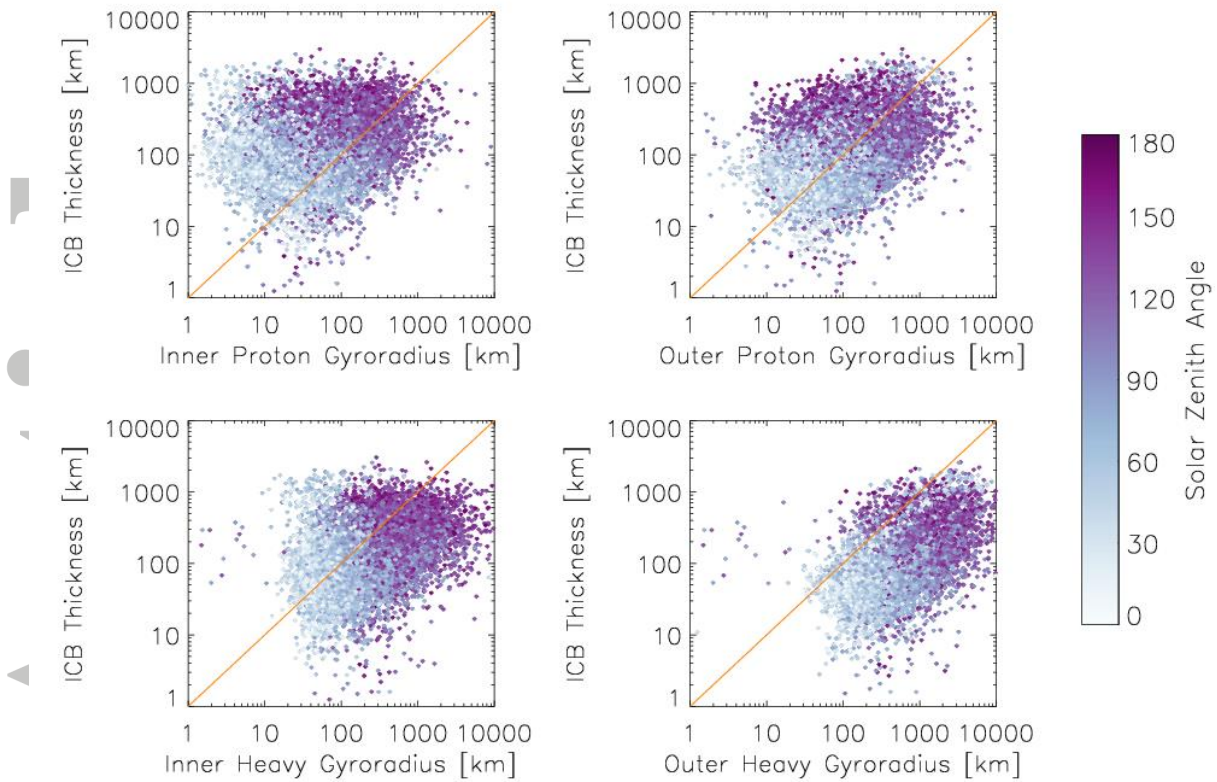


Figure 5: ICB thickness versus the proton (top row) and heavy ion (bottom row) gyroradii at the inner (left column) and outer (right column) edge of the ICB, with colors showing SZA. The orange lines indicate a 1:1 ratio.

Accepted

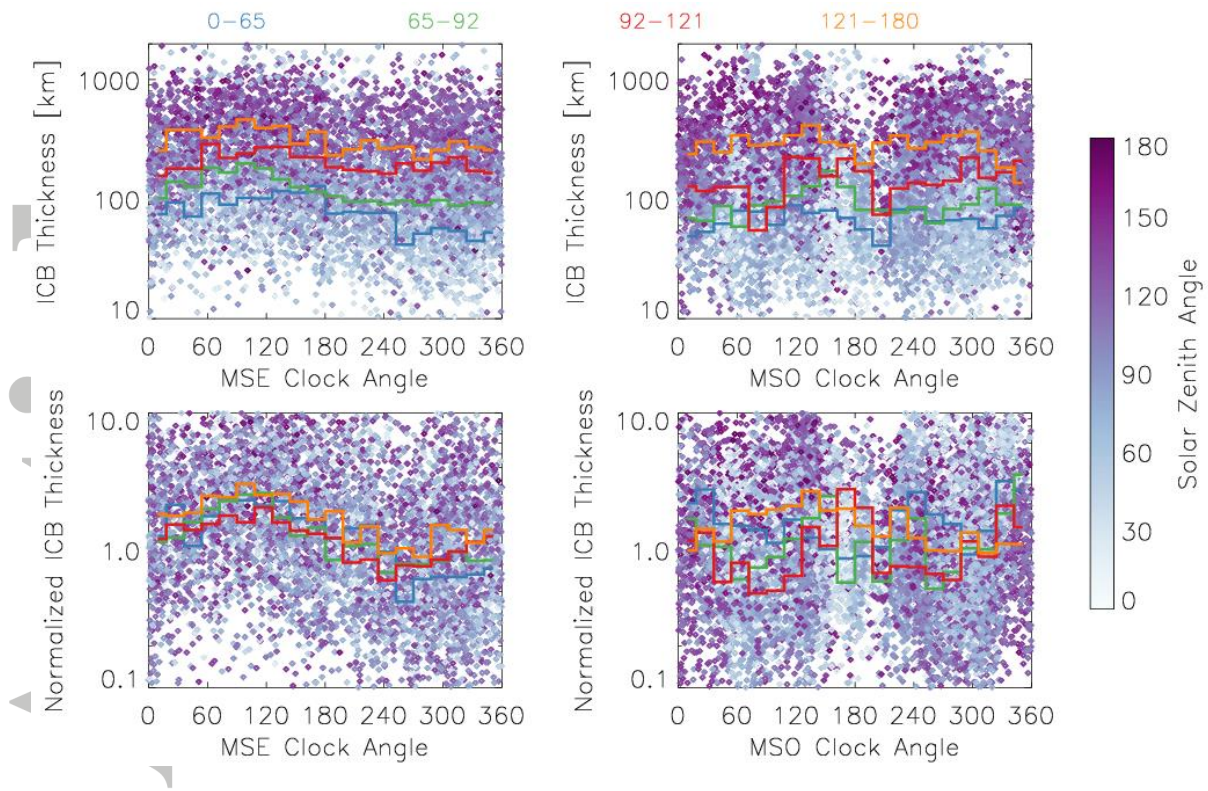


Figure 6: ICB thickness and ICB thickness normalized by the proton gyroradius at the outer edge of the ICB, as a function of the clock angle from the MSE y-axis (left column, only orbits during which we also measure the upstream magnetic field) and the clock angle from the MSO y-axis (right column, all orbits). The $+E_m$ direction lies at an MSE clock angle of 90° , and the $-E_m$ direction lies at an MSE clock angle of 270° . The colors of the points indicate the SZA of each crossing (as shown by the color bar), and the blue, green, red, and orange lines indicate median ICB thicknesses for four SZA quartiles.

Accepted

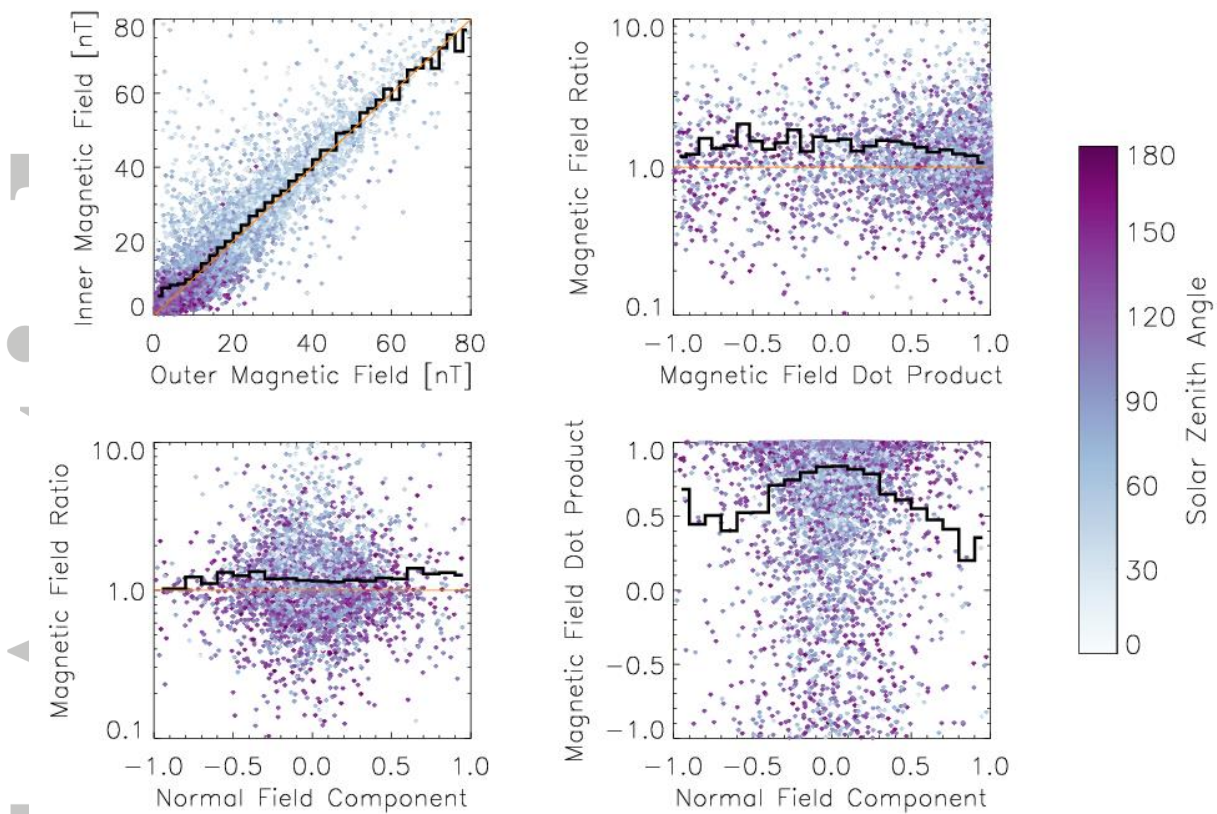


Figure 7: Magnetic field magnitudes at the inner and outer edge of the ICB (upper left), the ratio of the inner to outer field magnitude versus the dot product between unit vectors in the directions of the inner and outer fields (upper right), the field ratio versus the normal component of a unit vector in the direction of the field at the center of the ICB crossing (bottom left), and the inner-outer dot product versus the normal field (bottom right). The colors of the points indicate the SZA of each crossing (as shown by the color bar), and the dark black lines show average values. The orange lines indicate either 1:1 ratios (top left) or unity (upper right and bottom left).

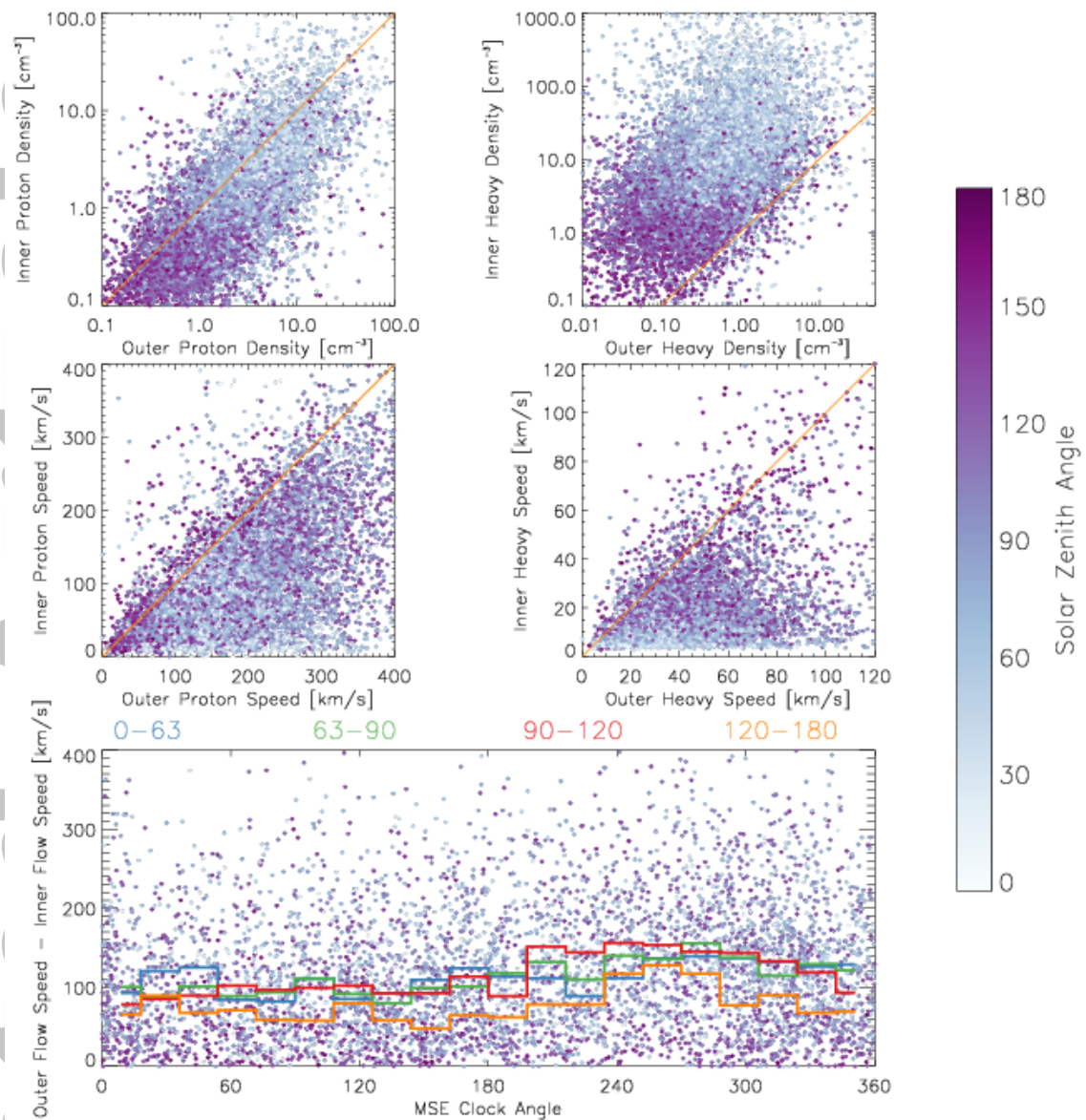


Figure 8: Proton and heavy ion density and speed at the inner and outer edges of the ICB, and the difference in average (proton + heavy) ion flow speed between the inner and outer edges of the ICB as a function of the clock angle from the MSE y-axis (only for orbits during which we also measure the upstream magnetic field). The colors of the points indicate the SZA of each crossing (as shown by the color bar), and the blue, green, red, and orange lines in the bottom panel indicate median flow speed differences for four SZA quartiles. The orange lines in the top four panels indicate 1:1 ratios.

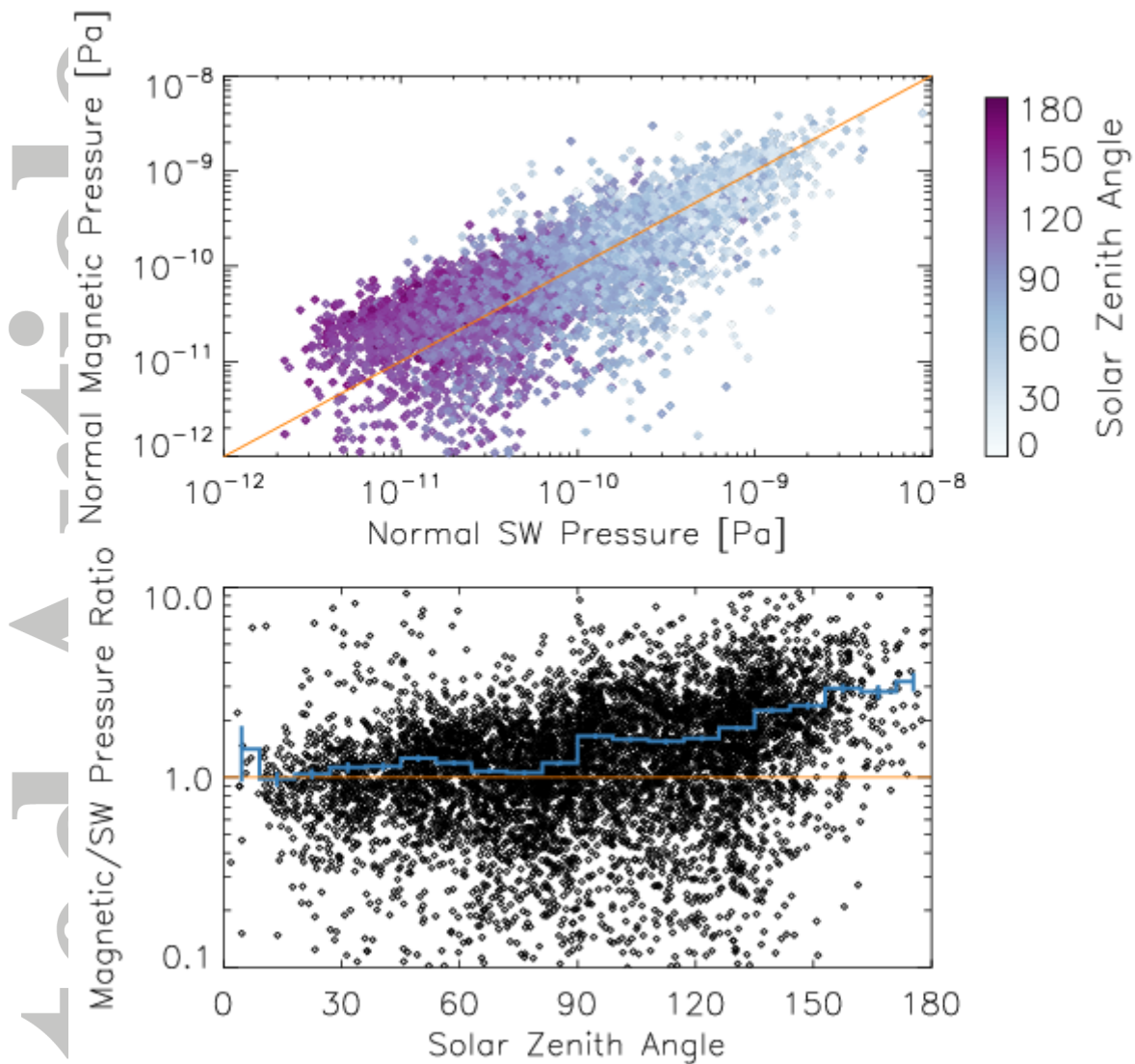


Figure 9: Normal magnetic pressure versus the normal component of the incident solar wind pressure at the ICB, and the ratio between them as a function of SZA. The colors of the points in the top panel indicate the SZA of each crossing (as shown by the color bar). The orange line in the top panel indicates a 1:1 ratio. The blue line in the bottom panel indicates the average ratio as a function of SZA, and the orange line indicates unity. Vertical blue lines in the bottom panel show the standard deviation of the mean value for each SZA bin.

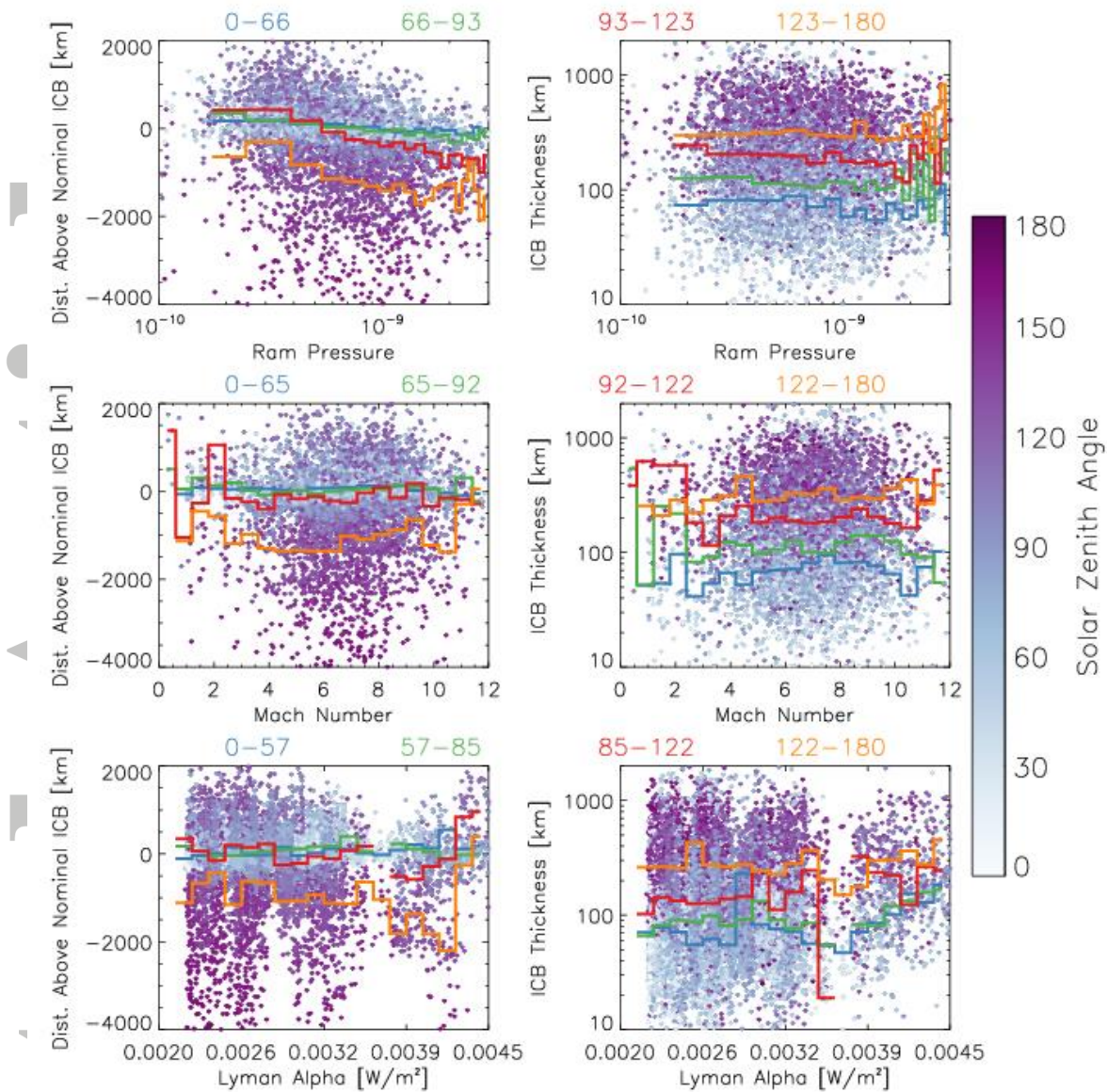


Figure 10: The distance of ICB crossings above or below the nominal ICB surface of Fig. 3 (left column) and the ICB thickness (right column) versus solar wind ram pressure (top row), solar wind Mach number (middle row), and Lyman alpha irradiance (bottom row). The colors of the points indicate the SZA of each crossing (as shown by the color bar), and the blue, green, red, and orange lines indicate median values for four SZA quartiles.

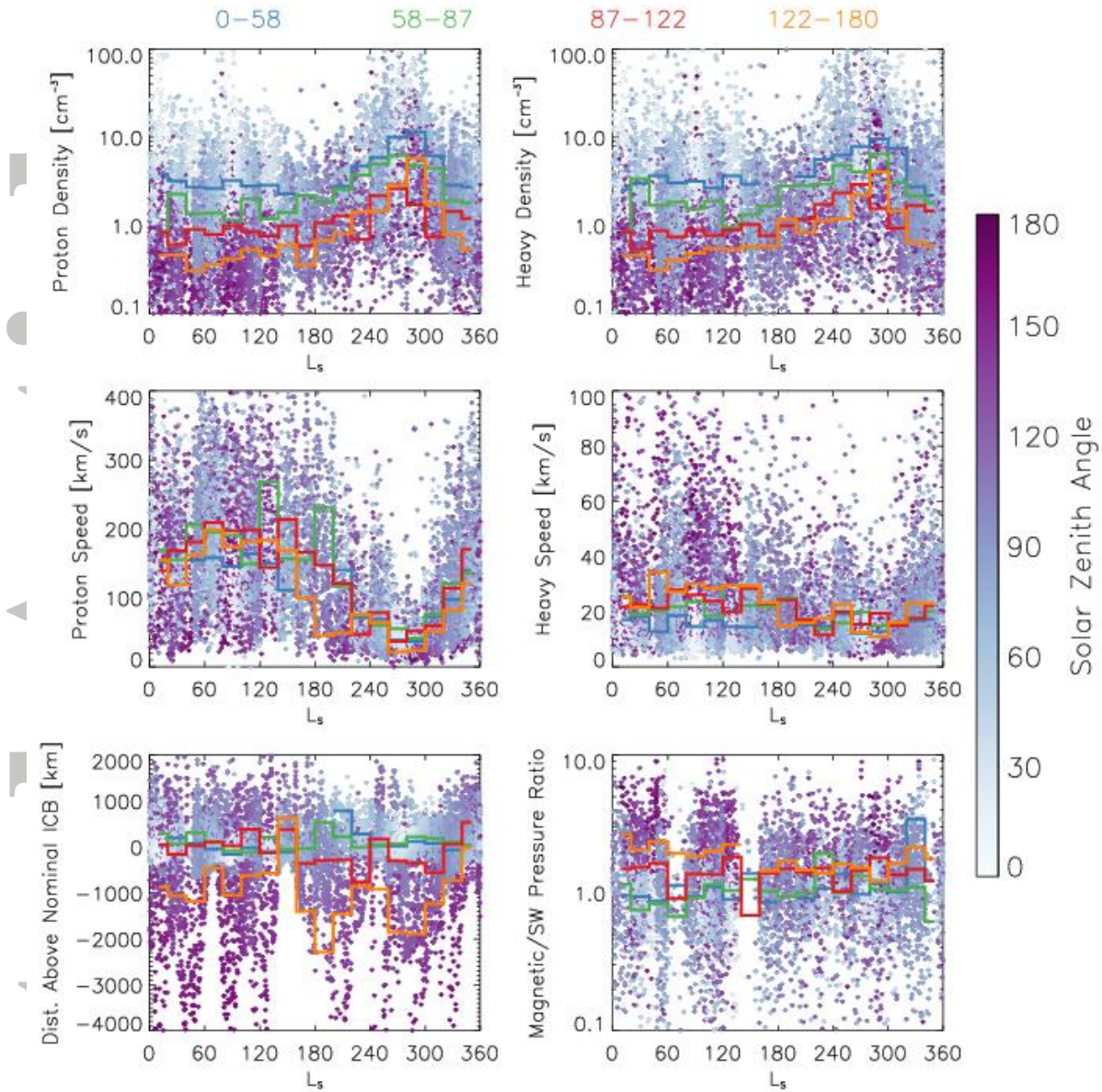


Figure 11: Proton and heavy ion density and flow speed, the distance of ICB crossings above or below the nominal ICB surface of Fig. 3, and the ratio between normal magnetic and solar wind pressure components at the ICB, versus Mars solar longitude L_s . The colors of the points indicate the SZA of each crossing (as shown by the color bar), and the blue, green, red, and orange lines indicate median values for four SZA quartiles.